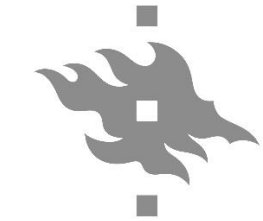

Master's thesis

The Department of Geosciences and Geography

Solid Earth Geophysics

Numerical Modelling of Oblique Subduction in the Southern Andes Region

Yijun Wang

2020

Supervisors:
David Whipp

Master's Programme in Geology and Geophysics

Faculty of Science

HELSINGIN YLIOPISTO
HELSINGFORS UNIVERSITET
UNIVERSITY OF HELSINKI
MATEMAATTIS-LUONNONTIETEELLINEN TIEDEKUNTA
MATEMATISK-NATURVETENSKAPLIGA FAKULTETEN
FACULTY OF SCIENCE

Tiedekunta – Fakultet – Faculty	Koulutusohjelma – Utbildningsprogram – Degree programme
Faculty of science	The Department of Geosciences and Geography

Opintosuunta – Studieinrikting – Study track

Solid Earth Geophysics

Tekijä – Författare – Author

Yijun Wang

Työn nimi – Arbetets titel – Title

Numerical Modelling of Oblique Subduction in the Southern Andes Region

Työn laji – Arbetets art – Level	Aika – Datum – Month and year	Sivumäärä – Sidoantal – Number of pages
Master's thesis	December, 2020	

Tiivistelmä – Referat – Abstract

The Southern Andes is an important region to study strain partitioning behavior due to the variable nature of its subduction geometry and continental mechanical properties. Along the plate margin between the Nazca plate and the South American plate, the strain partitioning behavior varies from north to south, while the plate convergence vector shows little change. The study area, the LOFZ region, lies between 38ºS to 46ºS in the Southern Andes at around 100 km east of the trench. It has been characterized as an area bounded by margin-parallel strike-slip faults that creates a forearc sliver, the Chiloe block. It is also located on top of an active volcanic zone, the Southern Volcanic Zone (SVZ). This area is notably different from the Pampean flat-slab segment directly to the north of it (between latitude 28º S and 33º S), where volcanic activity is absent, and slip seems to be accommodated completely by oblique subduction. Seismicity in central LOFZ is spatially correlated with NE trending margin-oblique faults that are similar to the structure of SC-like kinematics described by Hippertt (1999). The margin-oblique faults and rhomb-shaped domains that accommodate strain have also been captured in analog experiments by Eisermann et al. (2018) and Eisermann relates the change in GPS velocity at the northern end of LOFZ to a decrease in crustal strength southward possibly caused by the change in dip angle.

This project uses DOUAR (Braun et al. 2008), a numerical modelling software, to explore the formation of the complex fault system in the LOFZ in relation to strain partitioning in the Southern Andes. We implement the numerical versions of the analog models from Eisermann et al. (2018), called the MultiBox and NatureBox models to test the possibility to reproduce analog modelling results with numerical models. We also create simplified models of the LOFZ, the Natural System models, to compare the model displacement field with deformation pattern in the area.

Our numerical model results in general replicate the findings from MultiBox experiment of Eisermann et al. (2018). We observe the formation of NW trending margin-oblique faulting in the central deformation zone, which creates rhomb-shaped blocks together with the margin-parallel faults. More strain is accommodated in the stronger part of the model, where the strain is more distributed across the area or prefers to settle on a few larger bounding faults, whereas in the weaker part of the model, the strain tends to localize on more smaller faults.

The margin-oblique faults and rhomb-shaped domains accommodating strain is not present in the Natural System models with and without a strength difference along strike. This brings the question about the formation of the complex fault system in both the analog models and our numerical versions of them and hypothesis other than a strength gradient could be tested in the future.

Avainsanat – Nyckelord – Keywords

Lithosphere, crust

Säilytyspaikka – Förvaringställe – Where deposited

Muita tietoja – Övriga uppgifter – Additional information

CONTENTS

1. INTRODUCTION

Subduction is a crucial part of the Wilson cycle plate tectonic model (Wilson, 1966), which describes the cycle of opening and closing of oceanic basins through rifting, plate diverging and converging, etc. At a subduction zone, two plates are converging towards each other (Figure 1a). One plate is forced to bend at an angle beneath another plate due to gravity forces, which may trigger deformation at the plate boundary and in the overriding plate. Research on subduction systems is crucial for the society to reduce the impact of geohazards such as earthquakes, tsunamis, volcanic activities, etc., that are usually associated with plate convergence and subduction zones. Understanding the structures and tectonics of subduction systems also helps locate sedimentary basins and magmatic activities that are a possible host or source of natural resources such as hydrocarbons and ore deposits.

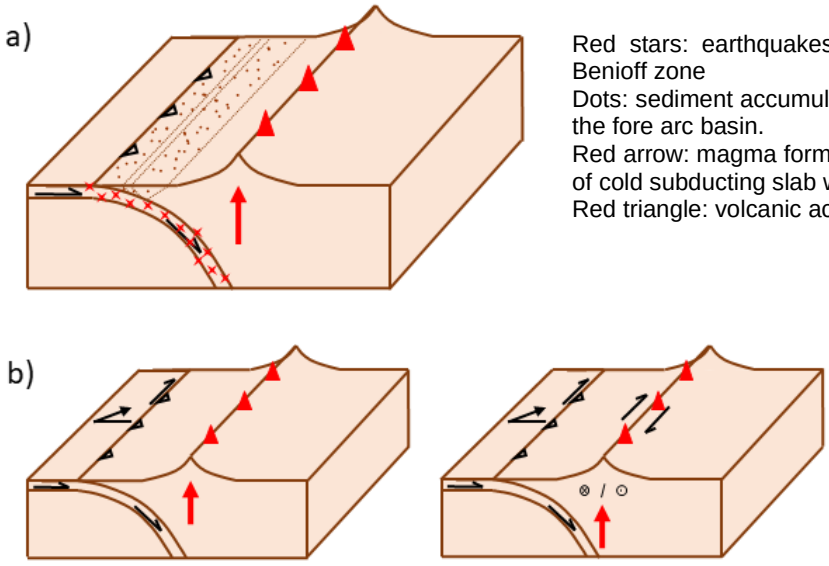

Figure 1 a) Drawing of a typical subduction system. b) Two scenarios of strain partition at an oblique subduction zon.e Left: the convergence vector is completely taken at the subduction interface by oblique thrust. Right: the trench normal vector is consumed at the subduction interface and the trench parallel vector is accommodated by a strike-slip fault system located near the volcanic arc.

Friction between the down-going oceanic slab and the upper plate builds up stress when the movement is locked along their interface and releases the stress during an earthquake event (Barazangi and Isacks, 1978; Lallemand et al. 2005). Most of the earthquakes including the largest and deepest ones occur in subduction zones, the strongest earthquake

being the M_w 9.5 1960 Valdivia earthquake at the South American subduction zone. The majority of subduction earthquakes are shallow and usually below 100 km depth, but they can also occur deeper as the subducted plate gets to hundreds of kilometers of depth. This zone marked by seismicity is called the Wadati-Benioff zone and can be used to locate the subducting slab (Benioff 1949). As these subduction earthquakes are usually related to an oceanic plate, they could also cause tsunamis, as the 1960 Valdivia earthquake did.

A volcanic arc usually forms in the upper plate 100 to 200 km away from the subduction trench with magma generated from interaction between the cold subducting slab and the mantle (Kearey et al. 2009), although they are not always present. In shallow or flat subduction systems, the temperature or pressure is usually not high enough to create melt that could rise up and form volcanos. During transport of material as subduction happens, the material fractionates by processes like dehydration, forming ore deposits as well as arc volcanism (Giggenbach 1992).

The most important characteristics of a subduction system that influence the type and degree of deformation in the upper plate include the plate convergence obliquity angle, the subducting slab dip, the age and strength of the converging plates. Most subduction systems are oblique (Philippon and Corti 2016), which means that the angle between the trench normal and the convergence velocity, the obliquity angle, is usually greater than 0. It is important to study the relationship between the geometry of the subduction zone and plate tectonics because strain introduced by oblique subduction could result in partitioning of the strain into a trench-parallel component, accommodated by strike-slip faults or shear zones in the over-riding plate, and a trench-normal component, consumed at the subduction interface by thrust faulting (Fig. 1). In an oblique convergence setting, strain can be fully accommodated at the plate interface by oblique thrusting or partitioned into a combination of its two components depending on the nature of convergence and physical properties of the converging plates (e.g., Fitch, 1972; McCaffrey, 1992).

The obliquity angle plays the major role in controlling strain partitioning behavior in the overriding plate. A high obliquity angle together with strong inter-plate coupling and a weak upper plate favors of strain partitioning (Fitch, 1972; McCaffrey, 1992; Nocquet el al., 2014). Fitch (1972) presents a simple model of strain partitioning between the

subduction interface and a strike-slip system parallel to the trench and shows that if the strength of both faults is equal, partitioning can occur at an obliquity angle greater than 45 degrees (Fig. 2). McCaffrey (1992) relates this critical angle where strain partitioning is possible to the arcsine of the ratio of resisting force on the plate interface and the potential strike slip fault in the upper plate.

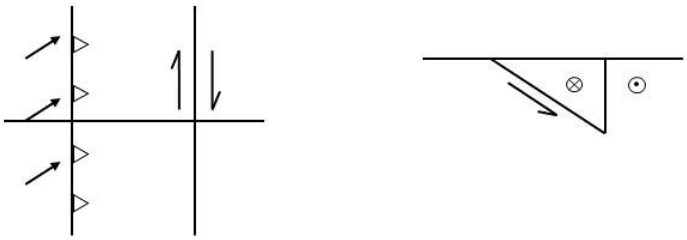

Figure 2. Simplified diagram showing the partition of the oblique convergence vector in a) map view and b) cross section view, adapted from Fitch et al. (1972)

The angle between the subducting slab and the horizontal surface, the dip angle, is another criterion to characterize the geometry of subduction. A subduction system with a dip angle of smaller than 30˚ or greater than 70˚ is called flat or steep subduction respectively. A young and less dense subducting slab often leads to flat subduction, in which it subducts normally until reaching a depth where the buoyancy force bends it towards a nearly horizontal dip (Stern, 2002; Lallemand et al. 2005; Van Hunen & Moyen, 2012; Kumar et al. 2016; Bishop et al. 2017; Manea et al. 2017). In contrast, an old and dense subducting slab usually results in a normal or steep dip angle due to the larger gravitational pull downwards. A good example is the Mariana Trench, where the oceanic crust is one of the oldest subducting oceanic crust on Earth. The dip angle is a secondary factor controlling strain partitioning in an oblique converging system. A shallow subduction dip is usually associated with a volcanic gap and thus a strong crust in the upper plate that is less favorable to accommodate strain, but the high buoyancy of this oceanic slab also creates a stronger coupling with the upper plate, which can promote strain partitioning (Dewey and Lamb, 1992).

Another factor that controls strain partitioning in a subduction zone is mechanical properties of the subduction system, especially the strength of the overriding plate and the coupling force between the converging plates (Ramos, 1999; Gutscher et al. 2000; Stern, 2002). The presence of a crustal weakness in the upper plate, such as pre-existing

fault system and/or volcanic zone, reduces the shear stress needed to initiate slip in the upper plate and thus facilitates strain partitioning. Many modern and ancient subduction systems show partitioned oblique convergence as strike-slip motion localized near the magmatic arc (Fitch, 1972; McCaffrey, 1992; Alvarado, et al. 2016). In addition, a strong plate coupling promotes the transfer and accommodation of stress in the overriding plate (Beck 1983; Jarrard 1986), and is associated with high friction at the plate interface, subducting a slab with rough topography such as ridge or seamount, or subducting young and buoyant material with a low dip angle. However, subduction zones with a low dip angle are associated with a lack of volcanism (Barazangi and Isacks, 1978; Dewey and Lamb, 1992) which makes the crust stronger than in the presence of a volcanic arc, where the strength could be overcome more easily by accumulated elastic strain. This is a good example that shows that any of these factors alone does not control strain partitioning and that we are looking at the net effect or interaction of the both the geometry and mechanical properties of the subduction system to study the behavior of strain partitioning.

The study area of this paper is the Liquiñe-Ofqui Fault Zone (LOFZ) in southern Central Andes. It is a strike-slip fault system located on top of the Southern Volcanic Zone (SVZ) in an active subduction zone where the Nazca plate and the Antarctic plate are subducting beneath the South America plate. There are signs of partitioned strain within the LOFZ, including slip on a series of margin-oblique and margin-parallel fault structures that are interconnected and on the master branches of faults that bound the area (Perez et al. 2016; Sielfeld et al. 2018), and a northward motion of the fore arc sliver (Beck et al. 1993). This low obliquity angle (20˚) is more unlikely to produce strain partitioning behavior of the two end member types (Figure 1), rather than a complex system as in the LOFZ that is the result of multiple factors interacting with each other. With the power of numerical modelling to manipulate subduction geometry and material properties, this paper studies strain partitioning in the LOFZ area by 1) testing the possibility to reproduce earlier analog modelling results with numerical modelling methods, and 2) creating simplified models of the LOFZ and experimenting with boundary conditions and crustal mechanical properties.

2. GEOLOGIC BACKGROUND

The Andes mountain range is one of the most prominent and longest subduction plate boundaries around the globe. Its origin is related to the separation of the Pangaea supercontinent and the formation of the Mid Atlantic Oceanic Ridge during the Triassic, which forced the Phoenix, Farallon and Nazca plates to subduct beneath the South American plate (Cobbold et al. 2007; Müller et al. 2019). The modern features of the Andes mountain range formed by tectonic activity during the Cenozoic (Oncken et al. 2006). Based on first-order variations in geologic features and tectonic histories, a division of the Andes into the Northern Andes (12˚N-3˚S), the Central Andes (3˚S-47˚S) and the Southern Andes (47S-56˚S) is widely used (Ramos, 1999). The Northern Andes records the collision and accretion of oceanic crust with the South American plate during the Mesozoic and early Cenozoic (Gansser, 1973; Ramos, 1999). The Central Andes is mainly the result of subduction and it has experienced uplift, crustal thickening, volcanism, migration of magmatism and seismicity related to subduction. There is almost no volcanic activity in the Southern Andes, and this area is characterized by a relatively high relief and a complex fold and thrust belt due to ridge collision (Ramos and Kay, 1992; Gorring et al. 1997)

Subduction parameters such as the obliquity angle, dip angle and physical properties of the plates vary along strike within all three segments of the Andes, which makes it the perfect place to study the relationship between subduction and upper plate deformation. There exist multiple sub-horizontal flat-slab segments and normal subduction segments from North to South in the Andes subduction zone. In the southern section of Central Andes, the Pampean flat-slab segment (27˚S to 33˚S) is characterized by foreland uplift, upper plate thickening, high intraplate seismicity and a lack of volcanism (Barazangi & Isacks 1976, Jordan et al. 1983). To the south of this flat subduction segment, seismic activity shows that the mean dip angle remains constant at 30˚ until around 42˚S and dips more steeply at 40˚ (Ramos et al. 1999) ~ 50˚ (between 44S and 45S, Pesicek et al. 2012) further south. The transition between flat and normal subduction can be gradual, accommodated by curvature in the slab as at the northern boundary of the Pampean flat-slab segment or abrupt, facilitated by slab tear at around 38˚S (Pesicek et al. 2012). This normal subduction segment extends from 33˚S to 46˚S up to the Chile triple junction between the Nazca, South America, and Antarctic plates and the subduction angle at this

region, which is also called the Patagonian volcanic gap, remains undetermined due to the lack of seismic and volcanic activities. South of the Chile triple junction, the convergence vector is nearly perpendicular to the trench.

The LOFZ is a narrow fault zone located around 100 km away from the trench ranging from 38˚S to 46˚S in Southern Andes (Fig. 3). It has also been characterized as an area bounded by margin-parallel strike-slip faults with dextral movement that creates a forearc sliver to the west, the Chiloe block. Other important structural elements related to the study area are: 1) the Nazca plate, subducting to the northeast at 66 mm/yr at an obliquity angle of 20˚ relative to the trench (Angermann et al. 1999); 2) the Antarctic plate, subducting nearly orthogonally to the plate boundary at 20 mm/yr south of 46˚S (DeMets et al. 1994); 3) the South America plate that overrides the two subducting oceanic plates; and 4) the Chile Triple Junction and the Chile Rise that are also subducting under the South American plate and mark the boundary between the Nazca and Antarctic plates. Approximately half of the convergence is accommodated as slip along the plate interface (Wang et al. 2007) and a major part of the plate convergence is released by earthquakes when the accumulated strain exceeds the strength of plates.

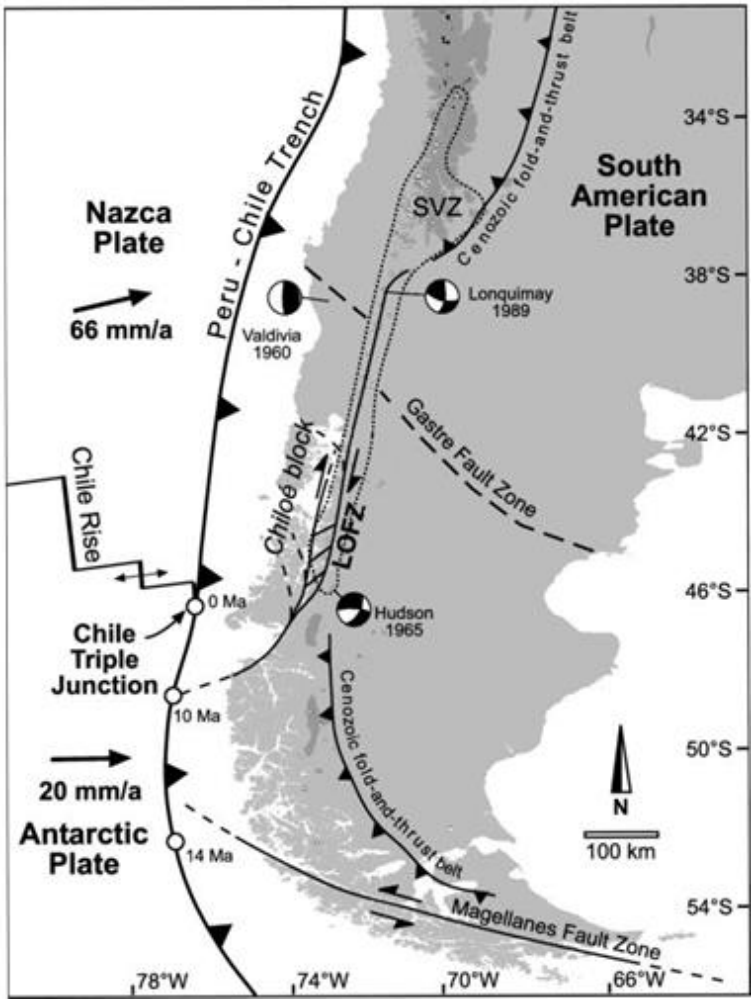

Figure 3. Map of study area (LOFZ), adapted from Rosenau et al. (2006)

Flat subduction segments along the Andes margin release 3 to 5 times more seismic energy than normal to steep subduction segments (Gutscher et al. 2000). In the forearc north of 38˚S near the LOFZ, GPS velocity observations are most prominently associated with interplate earthquake cycles. This shows that the oblique convergence vector in this segment is not partitioned into its trench-normal and trench-parallel components. On the other hand, south of 38S, the existence of trench-parallel strike-slip system and a Northward moving fore-arc sliver (Chiloe block) shows that there is a significant partitioning of convergence vector into the trench parallel component localized at the LOFZ (Hoffmann-Rothe et al. 2006). The Chiloe block is thus decoupled from the intra-arc and back-arc region and accommodates most of the strike-slip component of the transpression with a minimum amount of shortening (Lavenu et al. 1997; Diraison et al. 1998). The present strain partitioning of the LOFZ is accommodated by the main LOFZ branch and conjugate sets of short faults with a variety of directions and scales (Perez et al. 2016; Sielfeld et al. 2018).

Seismic data shows that the LOFZ is best characterized with 3 domains from north to south (Sielfeld et al. 2018): 1) a northern end where transtensional deformation dominates, characterized by splay faulting; 2) a central part where strike-slip dominates, at the trench-parallel, bounding branch of the LOFZ and at trench-oblique NE and NW trending faults that crosscut or connect the main branches; and 3) a southernmost part where transpression and strike-slip deformation dominates. The conjugate set of margin-parallel and margin-oblique dextral faults in the central section is similar to the structure of SC-like kinematics described by Hippertt (1999) (Fig. 4). These sets of short conjugate faults enclose a sigmoid-shaped domain that is less deformed and rotated, which could accommodate regional simple shear (Melnick et al. 2006a; Rosenau et al. 2006; Hernandez-Moreno et al. 2014). Based on this characterization, the kinematic constraints, including the total displacement in the LOFZ, long-term shear rate and vertical axis rotation have been estimated using a kinematic model, without knowing the exact displacement on each individual strand in the area (Rosenau et al. 2006). The result shows a smaller shear strain rate (~13 mm/yr) north of 40˚ S in LOFZ, compared to a larger shear strain rate (~32 mm/yr) in the southern LOFZ. This is compatible with partitioning nearly half of the oblique convergence in the intra-arc area in the northern LOFZ and complete partitioning in the southern LOFZ. The margin-oblique faults and rhomb-shaped domains have also been captured in analog experiments by Cembrano et al. (2005)

and Eisermann et al. (2018) and Eisermann et al. (2018) relates the change in GPS velocity at the northern end of LOFZ to a decrease in crustal strength southward possibly caused by the change in dip angle.

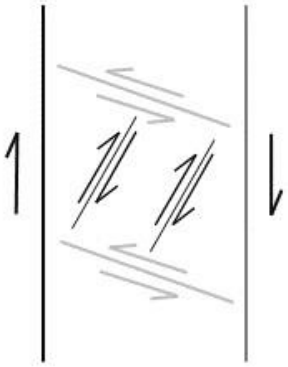

Figure 4. Simplified drawing of the SC-like structure adapted from Rosenau et al. (2006) and Hippertt et al. (1999).

The LOFZ is notably different from the flat-subduction segment of the Northern Andes where volcanic activity is absent. It is located on top of an active volcanic zone called the Southern Volcanic Zone (SVZ), which lies 250—300 km east of the trench and between latitudes 33˚S and 46˚S. Apart from the change in subduction angle and presence of volcanism that coincides with the location of the LOFZ, crustal thickness also decreases from around 50 km 33˚S southward, to around 35 km at 46˚S (Cembrano and Lara, 2009). The high heat flow resulting from asthenosphere convection in normal subduction segment (Gutscher et al. 2002), together with the presence of volcanic arc as a weak zone and a thinner crust could lead to a weak crust, which is in favor of strain partitioning into the LOFZ.

2.1. Numerical Geodynamical modelling

Geodynamic processes such as plate convergence and subduction can be studied by observing the product of a combination of geological events in place at present and inferring what has happened in the past. However, most geological structures are too large to observe, and the timescale of geologic events is usually long, which makes it impossible to see directly the changes while the event is occurring. Most natural systems are subject to a combination of processes and it is usually hard to identify the effect of a

specific process in the region. Analog and numerical models allow us to observe deformation in a smaller length and time scale with a relatively simplified representation of the natural system. Both techniques provide a controlled physical environment for us to model certain types of geologic processes.

Deformation in an analog model can be analyzed by taking photos of the top surface or cross sections in a desired direction at successive time and tracing the features either by hand or with image processing tools (Schellart 2017). Numerical models can be observed in any chosen cross section view or as a 3D block at any time, but the resolution of the observation is limited by computational power. The reliability of both modelling method is largely determined by the selection of materials and setup of the experiment as a representation of their natural prototypes.

Physical model and analog model are names assigned to experiments that use materials to reproduce development of geological structures in a laboratory. Analog experiments are usually designed with simple geometric shapes which represent some geologic structures of interest in nature created within the modelling apparatus (Schellart et al. 2017). Common analogue materials include dry sand, clay and silicone (Eisenstadt et al. 2005, Schreurs et al. 2006, Reber et al. 2020) and they are used to simulate the crust, the mantle or other types of rock. The physical properties of these materials each replicate some features of crust and mantle and can be scaled to simulate structure evolutions in the laboratory at a time and length scale that can be directly studied by human (Hubbert 1937). Analogue models have been used to analyze evolution of a wide variety of geological structures, such as strike-slip faulting (Viola et al. 2004), shortening and extension (Schreurs et al. 2006).

The geometry of analog model design is usually simple (Schellart et al. 2017). The layers of the Earth’s are represented by horizontal layers and topographic variations as wedges as in Schreurs et al. (2006). The degree that the simplified model can be compared to natural system is controlled by how well the selection of materials are scaled and how representative the design is with respect to the natural system. With all possible materials and physical modelling apparatus, it is still difficult to control certain variables and processes that are crucial to structure formation in nature, such as temperature and rock

rheology. It is also not convenient to observe the development of structures in the middle of a modelling apparatus and quantitatively analyze the stress and strain across the deforming body. Another shortcoming of analog models is that the rigid box that bounds the deforming material does not allow material flux through its sides as in nature.

On the other hand, material properties and model geometries can be manipulated easily by changing parameter values and applying different physical equations in a numerical model (Burov et al. 2014). Numerical modelling provides a prediction of the evolution in a region, given an initial configuration, material properties and a set of rules that geodynamic processes obey. It also allows us to observe the desired variables throughout the experiment and at any time. In addition to the simple geometry and type of deformation an analog model can have, numerical models can host complex structures and include the effect of surface erosion, magmatism and heat advection, which cannot easily be incorporated into analog models. Change in physical values such as stress, strain rate, and pressure can be tracked in the model as well. However, the effect of boundary condition should also be considered when evaluating a numerical model result (Gerya, 2010).

Buiter et al. (2006) and Schreurs et al. (2006) (Fig. 5) compared results from eight numerical models and from ten analogue models of sandbox type both among themselves and between the two types of experiments. The numerical models succeed in replicating the overall evolution of the corresponding analogue models in both extension and shortening setting, while they are not able to achieve the exact end configuration of analogue experiments. The results are similar qualitatively, but in the quantitative sense, the number of structures that formed, the angle, spacing and length of such structures and when they started forming vary among different models. The degree of variation between the numerical modelling results is roughly the same as between analogue experiments.

Before the development of computer of high computational power and three-dimensional (3D) modeling, most theoretical assumptions are tested with two-dimensional (2D) models either in map or cross section view. The disadvantage of 2D models is that they may over-simplify the system and cannot handle movement and property changes in three dimensions, especially considering oblique subduction. This study aims at analyzing the

deformation in the upper plate of a subduction zone undergoing oblique thrusting, and this process can be better studied with a 3D numerical model. In this work, the aims are (1) to construct numerical models that use the Multibox experimental setup (Eisermann et al. 2018) to test whether their results are similar to those from analog models, and (2) to explore the strain partitioning behavior for regions similar to the LOFZ using 3D numerical models of oblique subduction based on the geometry of this region.

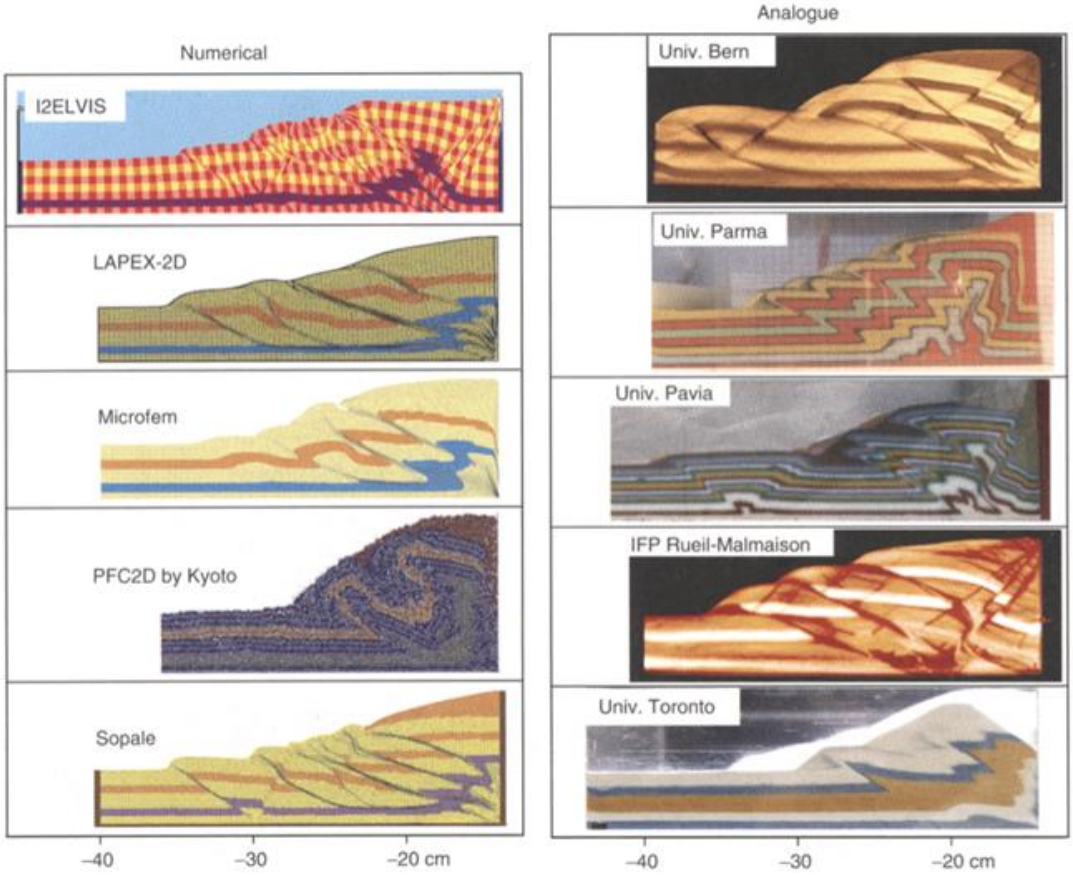

Figure 5. A comparison of numerical (left) and analog (right) model results from Buiter et al. (2006).

3. METHODS

3.1. Modelling software

The numerical modelling software used in this thesis is a thermomechanical modelling tool DOUAR (Braun et al. 2008; Thieulot et al. 2008). It is a 3D finite-element code designed to simulate viscous-plastic creeping-flow problems. DOUAR uses the Eulerian framework, which means that the reference frame is fixed in space, contrary to the

reference frame moving with the material (a Lagrangian framework). It can be used to model flow problems of mantle to crustal scale and solve force and thermal balance equations to determine the velocity field and temperature evolution throughout a 3D body. The main concepts of the code relevant to this study are explained below and a list of equations used by DOUAR can be found in Appendix A.

DOUAR uses the Finite Element Method (FEM) to approximate solutions to system of equations that describe the movement and change of physical properties in a 3D body. The FEM is based on dividing a 3D body into finite number of elements with a simple geometric shape (e.g., a cube) defined by its nodes. Values at the nodes can be calculated with predefined boundary conditions and the element geometry, while values inside an element are interpolated by using a shape function based on the geometry and values at the nodes. Increasing the number of elements normally increases solution accuracy, but also requires more computational power and time. Thus, the balance between accuracy and computational cost is crucial for designing numerical models using the DOUAR software.

Each material is assigned a material number and defined with a set of properties such as density, viscosity, thermal diffusivity, etc. Surfaces bound the space where a certain material number is assigned, and define the materials on both sides of it, including the air which is defined by the “free surface” in DOUAR (Fig. 6). Surfaces can be either fixed or free to move and deform and their position is tracked by the connected particles that make the surface. Materials can also be defined using Lagrangian tracking particles (cloud particles in DOUAR) that reside within the cubic finite elements defined by a Eulerian mesh. The particles drift through the model space following the velocity solution. The density and distribution of cloud particles can be dynamically adjusted during the calculation.

The code operates in time steps with a set of predefined materials, surfaces and boundary conditions. The relationship between time step and element size follows the Courant-Friedrichs-Lewy condition (Courant et al. 1928): $v * dt \leqslant C * dx$. With the courant number (C) equal to 0.5, the largest distance a particle can travel in our model during one timestep is less than one half of an element, which ensures the stability of the solution

and prevents unbounded error growth. The optimal time step size of a numerical model can be thus calculated using the boundary condition velocities and element sizes. At each time step, the velocity field and temperature change are calculated, and the surfaces and cloud particles are adjusted according to the solution.

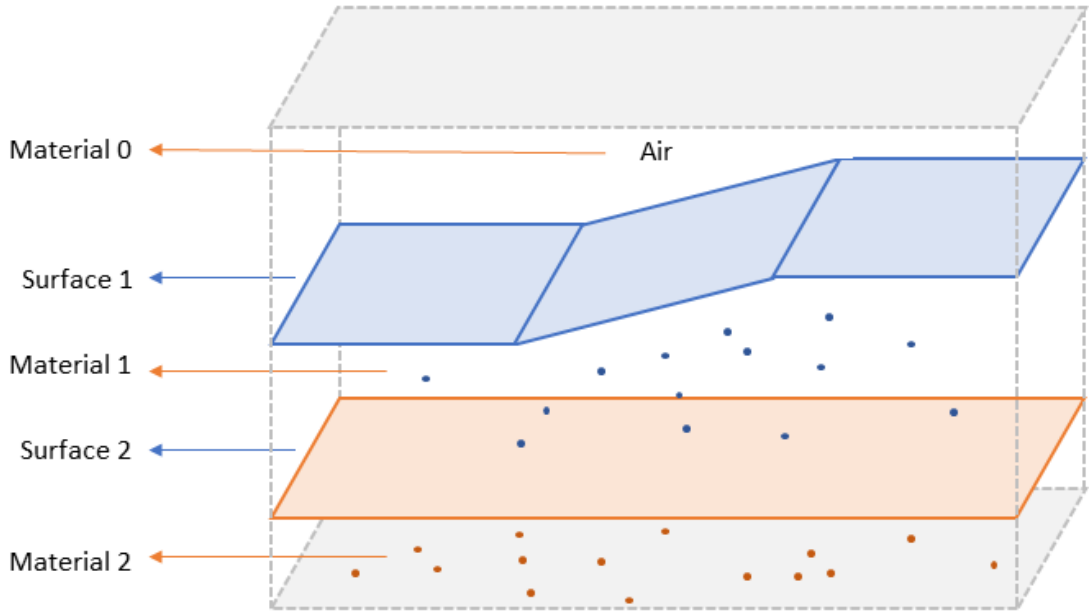

Figure 6. DOUAR surface and material definition (shown with cloud particles).

3.2. Model design

3.2.1. Numerical modelling of the MultiBox experiments

The overview of three sets of numerical models in this work and their relationship is shown in Figure 7. Three representative analog models from the Hamburg University analog experiment lab (Eisermann et al. 2018) with the same velocity boundary conditions but different crustal thicknesses as a proxy for crustal strength variations (Table. X) are tested in DOUAR as the “MultiBox” model set. The “NatureBox” models have the same geometry, but the physical parameters such as length, timescale and strength are scaled back to their natural equivalents (i.e., at the scale of the natural system, rather than the analog laboratory apparatus). The “Natural system” models are simplified models of the LOFZ fault zone at the same spatial scale as the NatureBox models that can be compared to the MultiBox and NatureBox results.

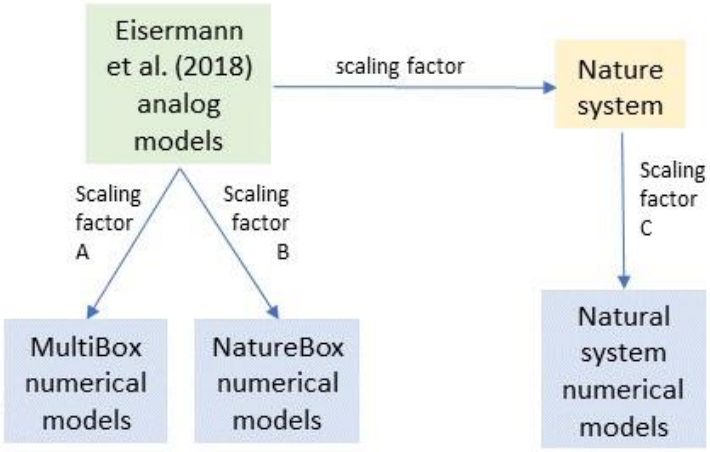

Figure 7. Model design.

The boundary conditions for MultiBox and NatureBox are shown in Figure 8 as a block diagram. It uses the geometry of the MultiBox apparatus (Eisermann et al. 2018), which is a box containing two halves each with assigned velocities in the x and y directions, simulating two plates colliding with each other. The analog materials fill the cubic space with a base of 100 cm * 69 cm and the box is driven by the piston beneath it and on its walls. Boundary velocities are directly applied to the right and left side together with the bottom surface in the numerical model as well. In the middle of the box there is initially a 27 cm gap between the piston where the velocities are applied. In the analog models, it is filled by nearly frictionless glass beads to allow dissipation of deformation at the velocity discontinuity, and in numerical model, no velocity is applied here to allow free slip. Empty space with no material and velocity is added on both left and right sides of the model in DOUAR to satisfy the requirement in DOUAR of creating a model with a square base. The location and width of piston and empty space in numerical model is defined by the model parameters sticky_x_min/max and pad_x_min/max respectively (Fig. 8).

Since it is difficult to apply a change in subduction angle in analog models, Eisermann et al. (2018) apply a change in crustal thickness to reflect the influence of change in slab dip from North to South (Eisermann et al. 2018). We expect the crust to be mechanically weaker above a normal subduction region, due to the presence of volcanism and crustal heat flow (Gutscher et al. 2000). Thickness on one section of the model (the southern part

in the strong-to-normal model and the northern part in the normal-to-weak model) is scaled to the calculated average crustal strength of the LOFZ ("normal", 0.05 cm thick) while the strength on the other side is either "strong" (0.09 cm) or "weak" (0.02 cm) (Fig. 9). This feature is implemented using the surface type 10 of the DOUAR free surface geometries (Fig. 10). The initial topography of the 3 MultiBox models can be found in Figure 9 and the layer thicknesses are shown in Table 1.

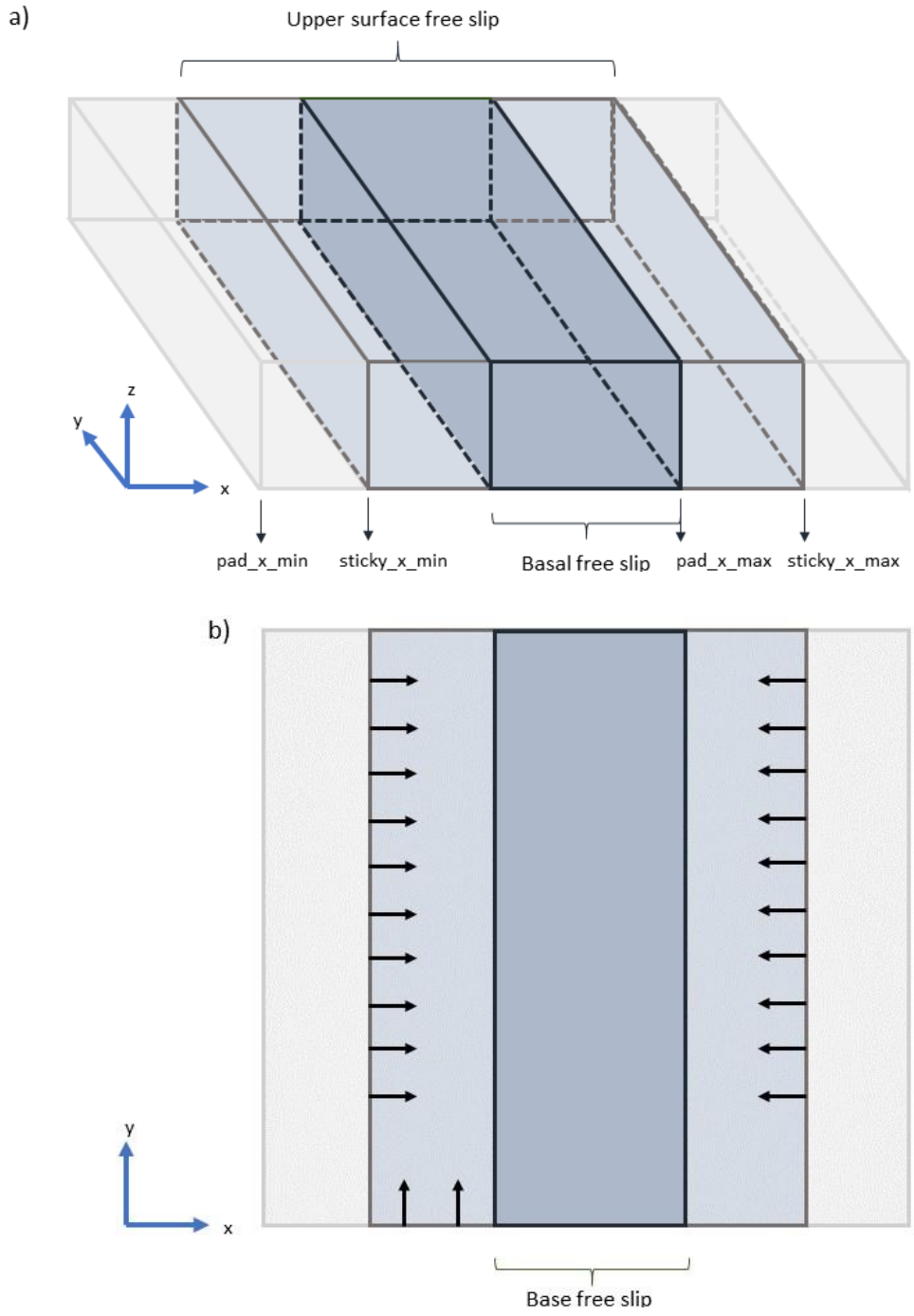

Figure 8. a) Block diagram of MultiBox and NatureBox model design. b) Map view of model design with velocity vectors

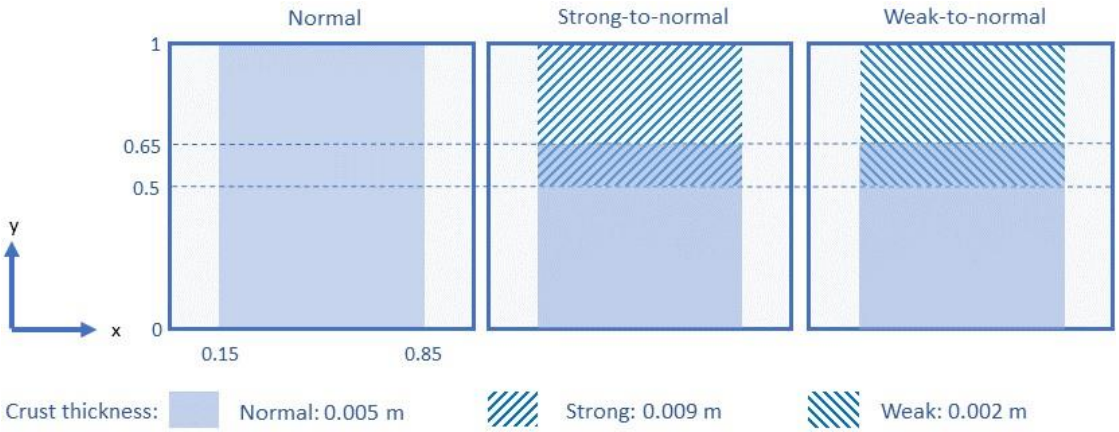

Figure 9. Normal, strong-to-normal and weak-to-normal model topography.

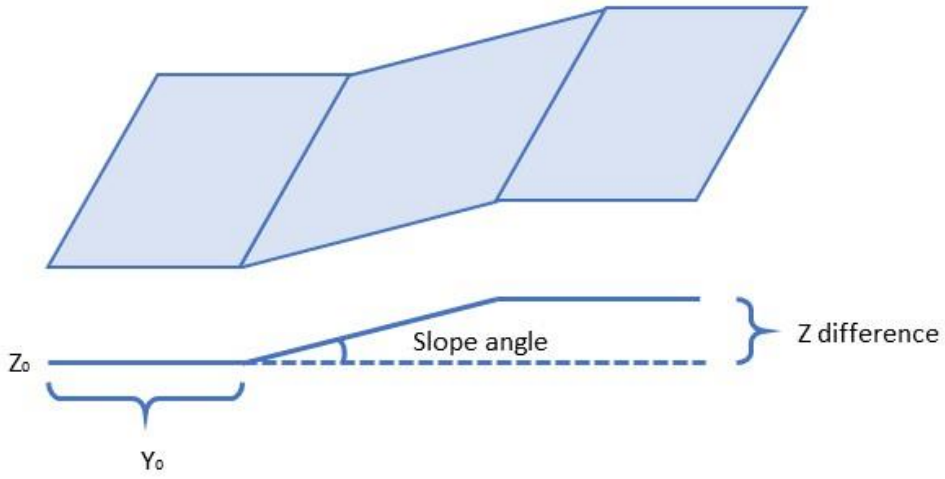

Figure 10. Surface type 10 with a ramp.

Table 1. Material Properties used in the model, adapted from Eisermann et al. (2018)

	MultiBox		**NatureBox**		**Natural System**		
	Material 1	**Material 2**	**Material 1**	**Material 2**	**Material 1**	**Material 2**	**Material 3**
Density (kg/m^3)	1560	1600	2500	2800	2500	2800	2500
Viscosity (Pa s)	1.5d11	1.5d5	1d28	1d22	1d28	1d22	1d28
Cohesion	1 Pa	1 Pa	1 Mpa	1 Mpa	1 Mpa	1 Mpa	1 Mpa
Friction angle	30	30	30	30	15	30	15
Approximate layer/rock	crust	mantle	crust	mantle	crust	mantle	weak zone

Similar to the MultiBox analog experiments, we use two materials to represent a brittle upper layer and a viscous lower layer in the numerical MultiBox models. Their material properties are shown in Table 2. The MultiBox models use the analog material properties and the NatureBox models use the properties of rock from which the analog materials are scaled.

Table 2. Scaling factors used in numerical modelling

DOUAR Scaling	**MultiBox**	**NatureBox**	**Natural System**
Length scale (km)	0.001	2000	1000
Velocity scale (km/Myr)	306600	30	66
Density scale (kg/m3)	1.6d3	2.8d3	2.8d3
Timestep (yr)	1.90128d-6 (≈1min)	38888.88888	38888.88888

In the MultiBox analog experiments (Eisermann et al. 2018), 1 hour is roughly scaled to 2.33 Ma in nature and each experiment to be reproduced is between 2.67 h to 3.17 h. The numerical models all run through 200 time steps and each time step can be scaled to 1 min in an analog model and 38.89 kyr in nature for MultiBox and NatureBox models respectively, which correspond to 3.33 h and 7.78 Ma at the end of the model. Other scaling factors used in the numerical models are shown below in Table 3.

Table 3. Model thickness

	brittle layer	**viscous layer**
MultiBox (m)		
Normal	0.005	0.03
Normal to Strong	0.009	0.03
Normal to Weak	0.002	0.03
NatureBox (km)		
Normal	10	60
Normal to Strong	18	60
Normal to Weak	4	60
Nature System (km)		
Oceanic plate	20	80
Continental Plate	40	60

3.2.2. Numerical Modelling of the LOFZ

The boundary conditions of a simplified of the LOFZ are shown in Figure 11, as a block diagram with velocity and material definitions. The box is 1000 * 1000 * 100 km^3 and it roughly represents the tectonic setting between 38˚S and 47˚S of the LOFZ region, including an obliquely subducting oceanic plate as a parabola on the west side, a stable continental plate on the east side and a crustal weak zone representing the active volcanic arc. The box covers more than 200 km to the west of the trench and 200 km to the east of the Southern Volcanic Zone (SVZ). The applied convergence vector is 66 mm/yr, with a 20˚ obliquity angle and the subduction dip angle is either 50˚ or 30˚ measured at the bottom of the model. The details of how the parabola surface is defined is shown in Appendix B. The material properties, scaling factors and layer thickness of the Natural System Models is in Table 1, 2 and 3 respectively.

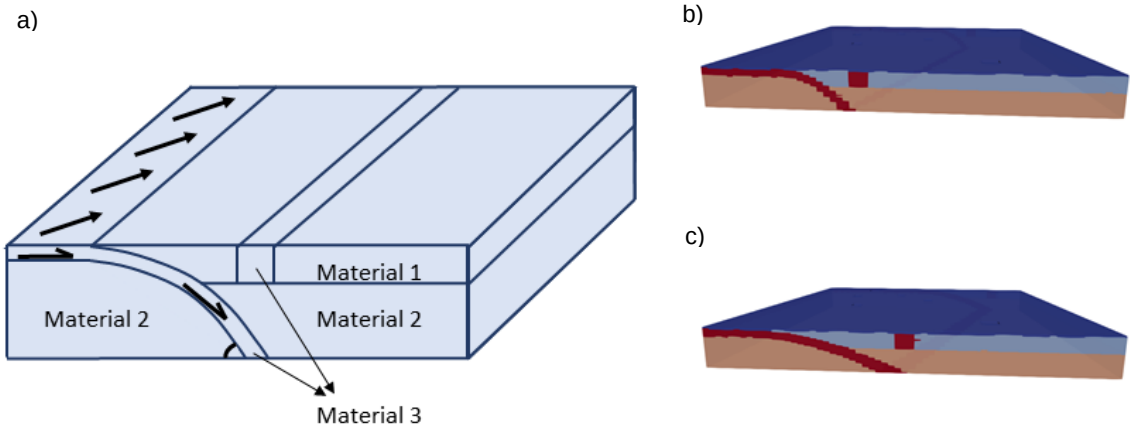

Figure 11. a) Block diagram showing the Natural System Model boundary conditions (not drawn to scale). Material 1 is crust, material 2 is mantle and material 3 is weak crust. Detailed material properties can be found in Table 3. b) 50 dip Natural System Model design. c) 30 dip Natural System Model design.

4. RESULTS

4.1. MultiBox Model Results

4.1.1. Topography

As shown in Figure 12, in all three MultiBox models, oblique convergence creates surface uplift above the free slip section with two anticlines uplifted on top of the two velocity discontinuities, which are the boundaries between the central free-slip section and the two

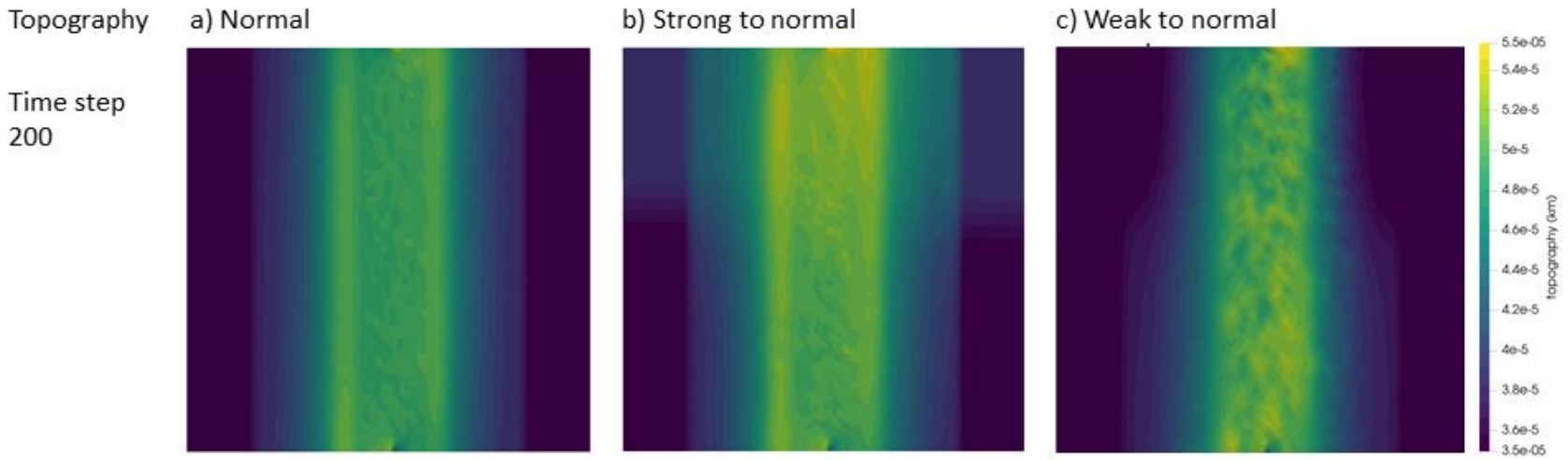

Figure 12. MultiBox models, vertical elevation above model base at time step 200.

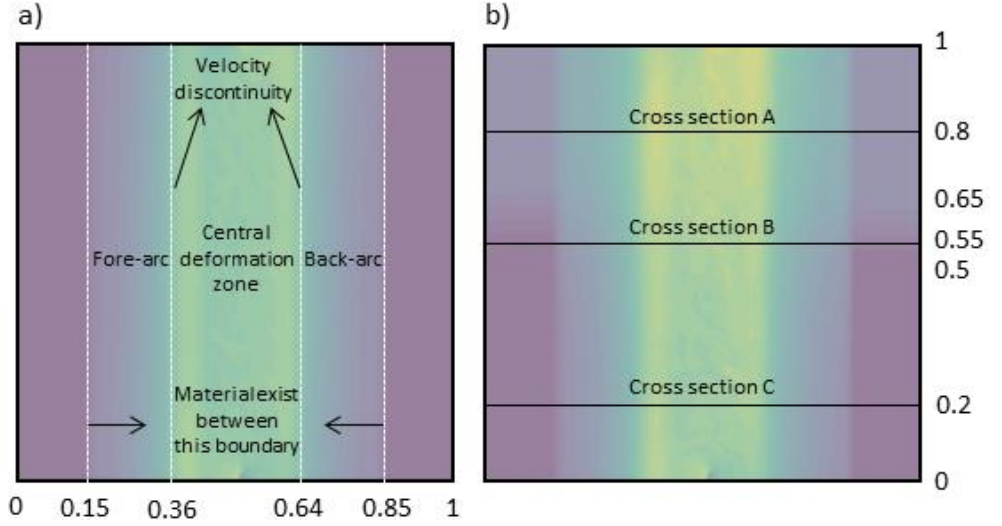

Figure 13. a) The fore-arc, back-arc and central deformation zone are labelled here within their boundaries (white dashed line). The locations of boundaries are labelled along the southern side of the box. b) Locations of cross sections taken in the model. Their distance to the southern boundary of the model is labelled along the eastern side of the box. Both the MultiBox and NatureBox models use this set of terminology to refer to regions and cross sections.

parts on the outer sides where a constant velocity is applied (as labeled in Figure 13). At the end of the model (200 time steps), roughly equivalent to 200 minutes of deformation in the analog MultiBox experiment, the central uplifted section is about 0.048 m above the original top surface and the maximum uplift at the anticline is about 0.05 m, while the eastis slightly higher. The strain rate taken at an E-W cross section in the middle of the box (Figure 14, cross section B as in Figure 13) shows two pop-up structures that are related to the formation of the central uplift. Two orogenic wedges have formed in the fore-arc and back-arc region to the outside of the central plateau. These structures accommodate the most shear strain apart from the shear zones in the middle of the model.

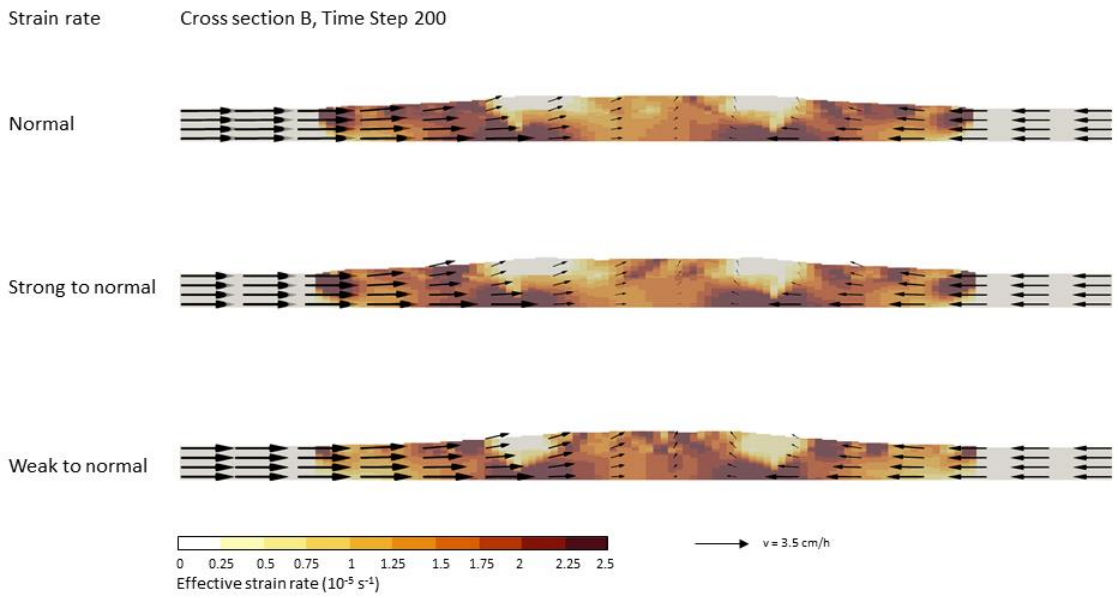

Figure 14. MultiBox models, strain rate with velocity vectors at time step 200 on cross section B.

4.1.2. Strain rate and total strain

There are traces of structures with a trench-oblique, northwest trend that seem to crosscut the central deformation zone (Figure 15). Comparing the result at 150 minutes to 200 minutes, strain is more distributed at an early stage and tends to localize more into these oblique faults as the model evolves. The accumulated strain is distributed evenly in the free slip zone and the location where there is slightly higher total strain match the trace of oblique faults observed with higher strain rate (Figure 16). These margin-oblique

structures could be faults that form temporarily to accommodate oblique convergence and get reorganized throughout time. They fail to grow into a North-South oriented master

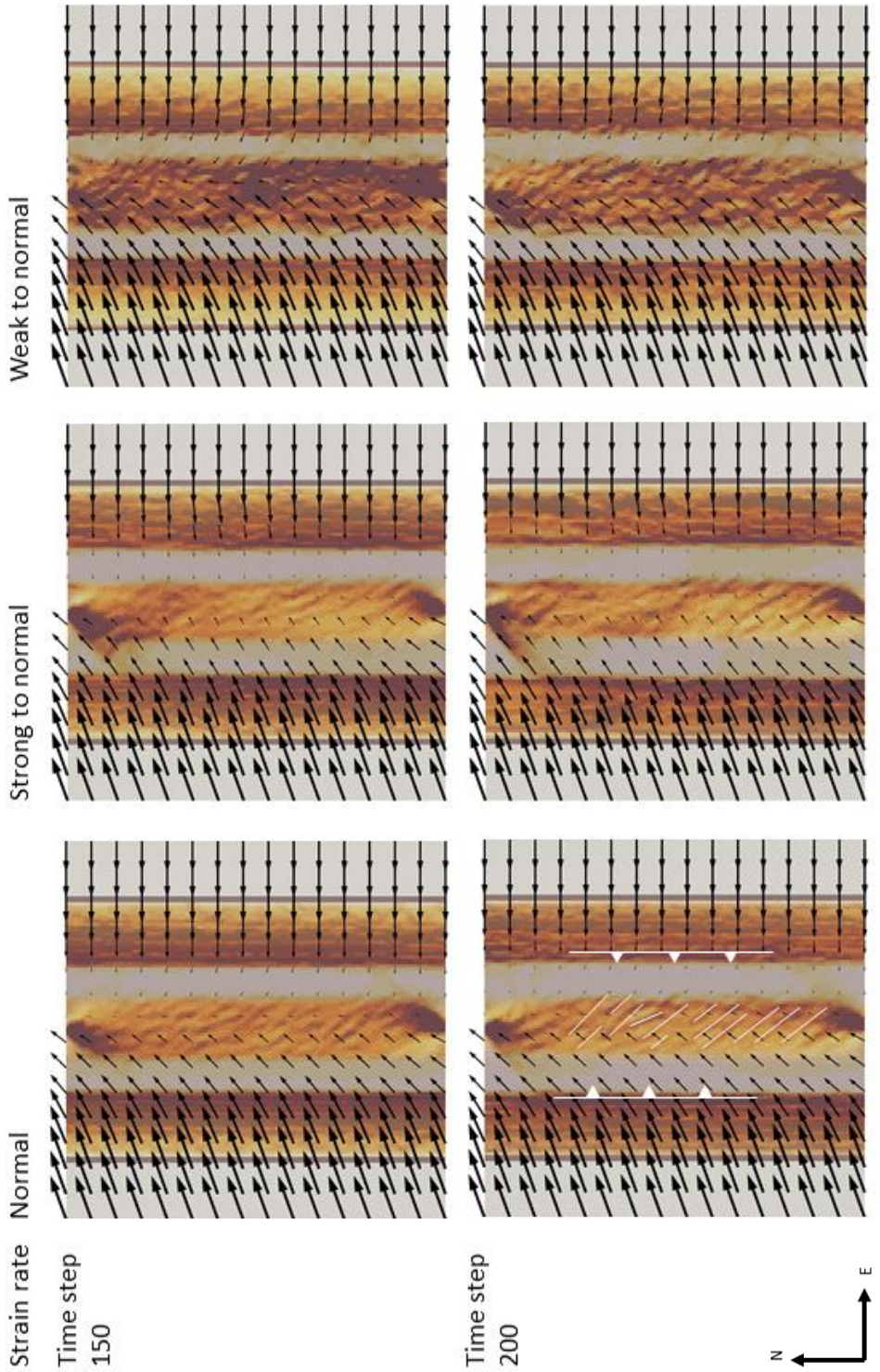

Figure 15. MultiBox models, strain rate with velocity vectors at time step 150 and 200. Velocity vectors are scaled, and the boundary condition convergence velocity (3.5 cm/h) is shown as a reference. Margin-oblique faults in the central deformation zone and thrust fronts in the fore- and back-arc region are marked (white) in the normal model at time step 200 as a guide.

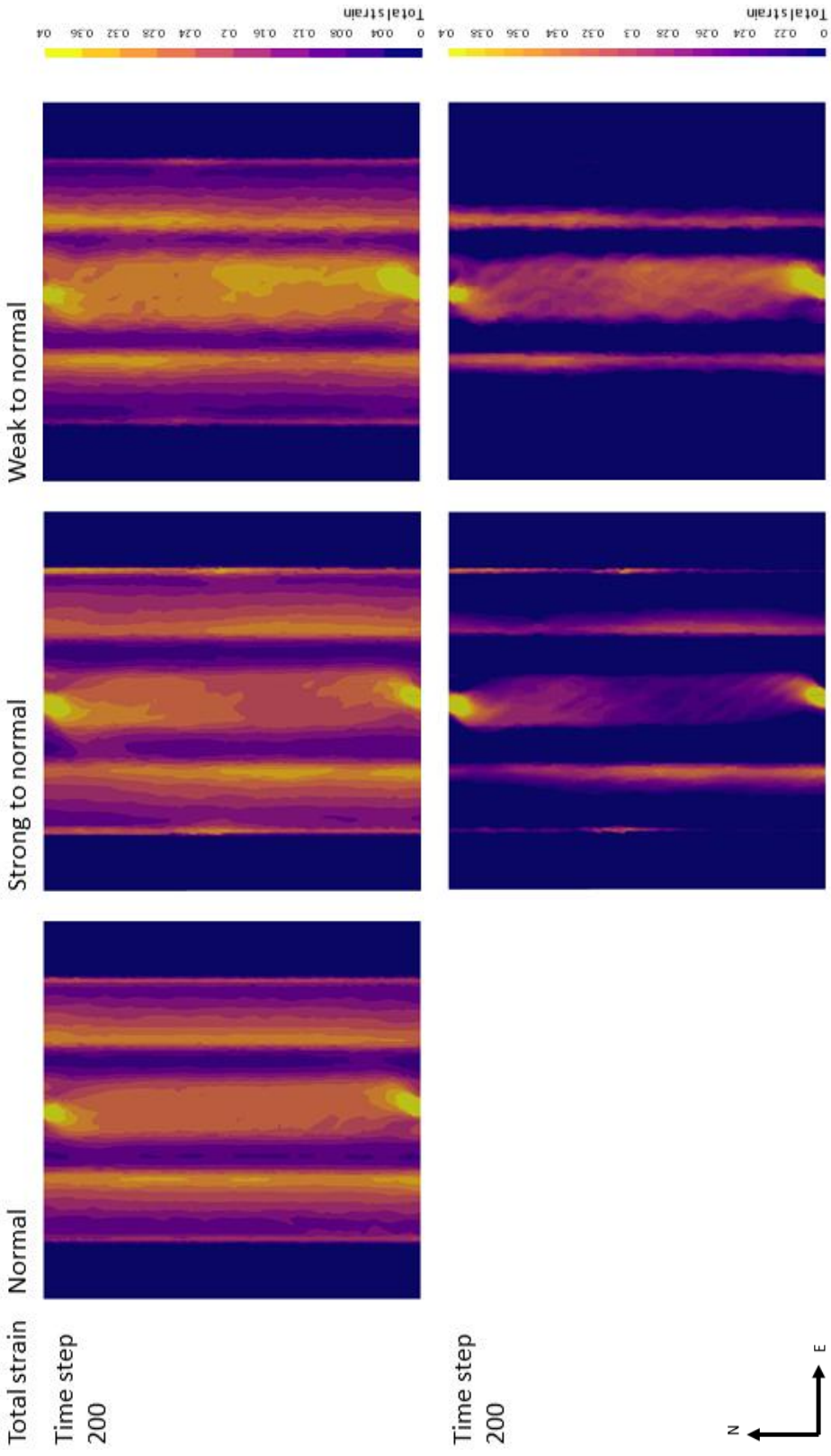

Figure 16. MultiBox models, accumulated strain at time step 200. A color bar with a different range is applied to the models with strength gradient to show the margin-oblique structures more clearly.

fault at the boundary of high strain region in the middle of the central shear zone at the end of the model.

Strain rate, total strain and velocity vectors in the normal model do not generally vary along-strike, in contrast to the models where the thickness of the crust (a proxy for strength) varies from north to south. In the model where there is a strong northern section transitioning into a normal strength section in the south (strong-to-normal model), the displacement pattern appears different (Figure 15). More strain is accommodated in the stronger part (Figure 16). At the same time, strain is more distributed across the central deformation zone and accommodated in the bounding faults in the stronger section, while it is more localized into distinct oblique faults that crosscut the central deformation zone in the weaker section (Figure 16). Similarly, in the model where the strength increases from weak in the north to normal in the south (weak-to-normal model), more strain is accommodated by the normal strength section, but the margin-oblique fault system is not as clearly-defined as in the strong-to-normal model. The margin-oblique faults are present but are fragmented by short margin-parallel faults, forming rhomb-shaped domains together. The rhomb-shaped domains in the normal section appear to be larger and accommodates more strain than those in the weak section (Figure 15). The stronger section in both models accommodates more strain than the weaker part.

4.1.3. Orientation of velocity vectors

The orientation of velocity vectors is fairly uniform along North-South direction in the normal model without the strength gradient (Figure 15). To the west of the free slip section (fore-arc), the velocity is generally NE-oriented aligned with the applied velocity boundary condition, while the velocity vectors rotate counter-clockwise towards a northward motion closer to the central deformation zone, indicating the northward transport of material is greatest in the center, and is at its maximum near the east side of this zone. The northward velocity component also increases as the model develops. In the back-arc area to the east of the free slip section, the velocity points westward as is defined by the boundary condition, and it rotates towards a NW orientation approaching the eastern boundary of the central deformation zone.

As above, the orientation of the velocity vectors in the strong-to-normal and weak-to-normal models also differ along the y-axis. In the fore arc and the central deformation zone, the northward component is the smallest in the strong-to-normal model and is the largest in the weak-to-normal model (Figure 15). In the back arc, the velocity vectors point in a WSW direction with a small southward component in the region of thickness transition of the strong-to-normal model. This differs from the NW transport of material in the same region in the two other models.

From the velocity vectors in 3 E-W cross sections taken at different locations (cross sections A, B and C in Figure 13), we can see that generally the velocity pattern is similar along strike (Figures 17-19). The upward velocity (uplift rate) decreases from north to south as the velocity vectors rotate counterclockwise in the central deformation zone near the east velocity discontinuity in the strong-to-normal and weak-to-normal models (Figures 18 and 19). Across the velocity discontinuity in the back-arc region, the uplift rate increases from north to south and rotates clockwise, pointing almost directly upward in the weaker part. This along-strike variation of vertical velocity is absent in the normal model (Figure 17).

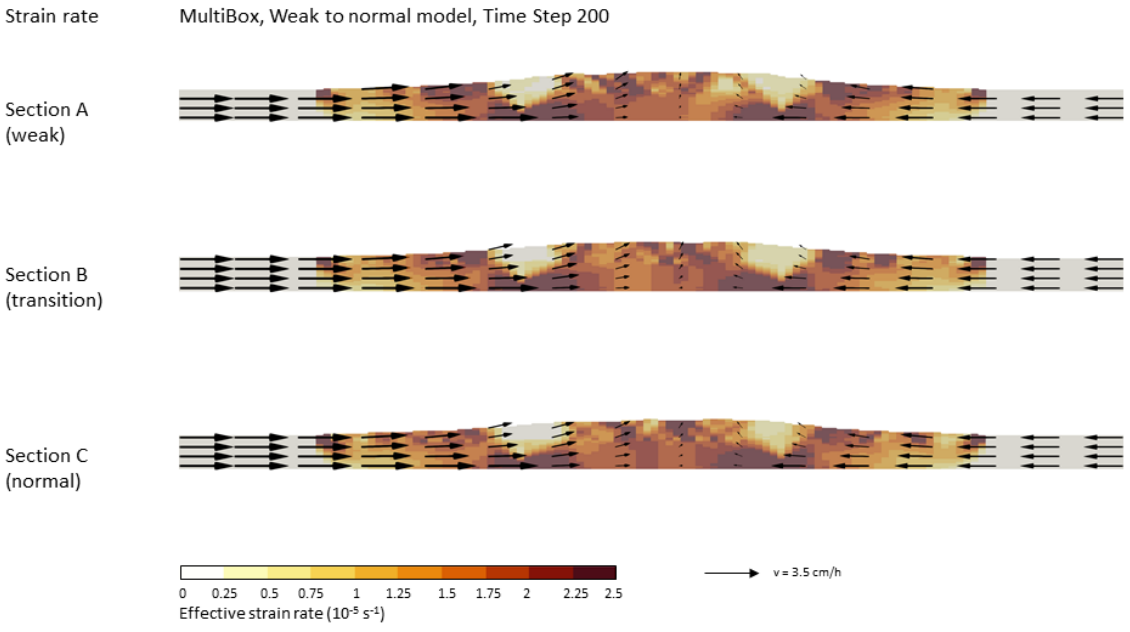

Figure 17. MultiBox models, cross sections A, B and C from the normal model with velocity vectors overlaying the strain at time step 200.

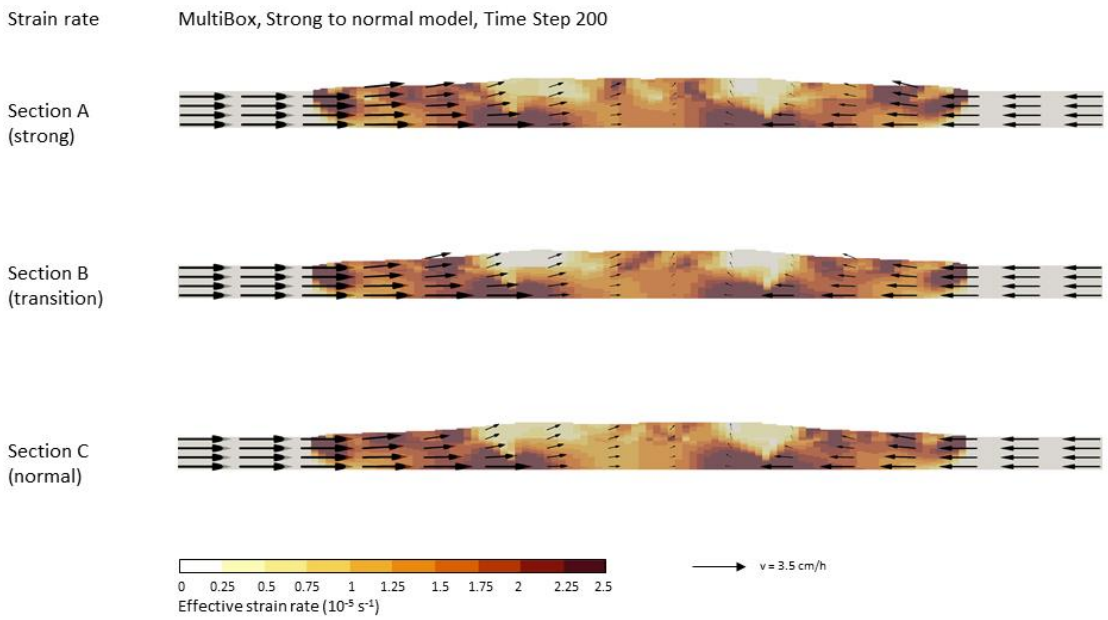

Figure 18. MultiBox models, cross sections A, B and C from the strong-to-normal model with velocity vectors overlaying the strain at time step 200.

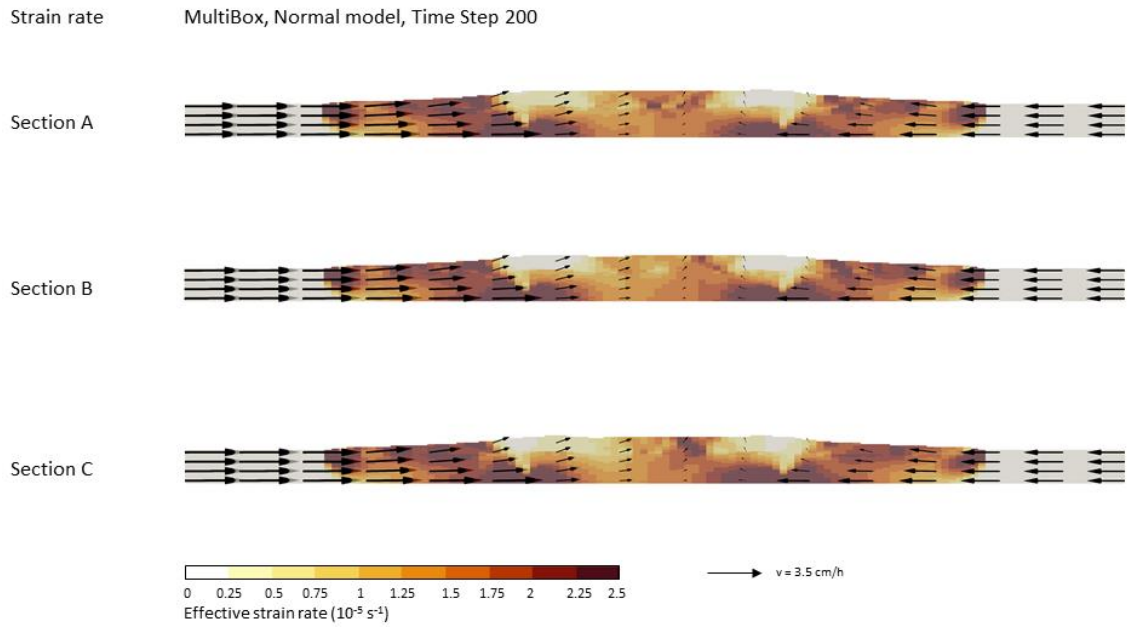

Figure 19. MultiBox models, cross sections A, B and C from the weak-to-normal model with velocity vectors overlaying the strain at time step 200.

4.2. NatureBox Model Results

The development of topography in the NatureBox models is similar to that observed in the MultiBox models, where the central deformation zone is uplifted, and the elevation

decreases on both sides of it until reaching the material boundary (Figure 20, regions as labelled in Figure 13). The central uplifted region reaches 110 km above the model base (40 km above the surface of the normal thickness section), after 200 steps of convergence, approximately 7.7 Myr, and the two anticlines on both sides of it are about 5-10 km higher (Figure 20). As in the MultiBox experiments, similar sets of thrust faults form a pop-up structure that is visible in the cross section at the middle of the model, only the strain is more localized on the thrust faults rather than being distributed towards the more distal fore arc and back arc regions (Figure 21). The orientation of velocity vectors on the map view (Figure 22) and in cross sections (Figure 21) is also similar to what we observed in the MultiBox models.

Also, as in the MultiBox models, the stronger section in NatureBox model accommodates more strain (Figure 23). However, a notable difference between these two sets of models is that the strain rate map shows a more complex series of margin-parallel and margin-oblique faults in the central deformation zone than in the MultiBox models. In the normal model, the margin-oblique faults could not grow to lengths that crosscut the deformation zone but are always cut by margin-parallel faults and enclose a rhomb-shaped area (Figure 22). In the strong-to-normal model, strain tends to be accommodated primarily by a margin-parallel fault on the left side of the central deformation zone in the strong section (Figure 22), while being more distributed in the normal section across several faults that also form the rhomb-shaped domains. Similarly, the stronger section (normal thickness) in the weak-to-normal model hosts fewer number of structures that accommodate more strain than the weaker section to the north of it (Figure 22).

4.3. Natural System Model Results

4.3.1. Strain rate

The Natural System models do not reproduce the margin-oblique fault systems as observed in numerical versions of the analog experiments. We observe that the strain rate is primarily accommodated at the subduction interface and is also taken by a nearly vertical fault that is spatially related with the weak zone in the continental crust or by a thrust fault that connects the subduction interface with the weak zone (Figure 24). Strain is distributed uniformly across the region between the trench and the weak zone and the

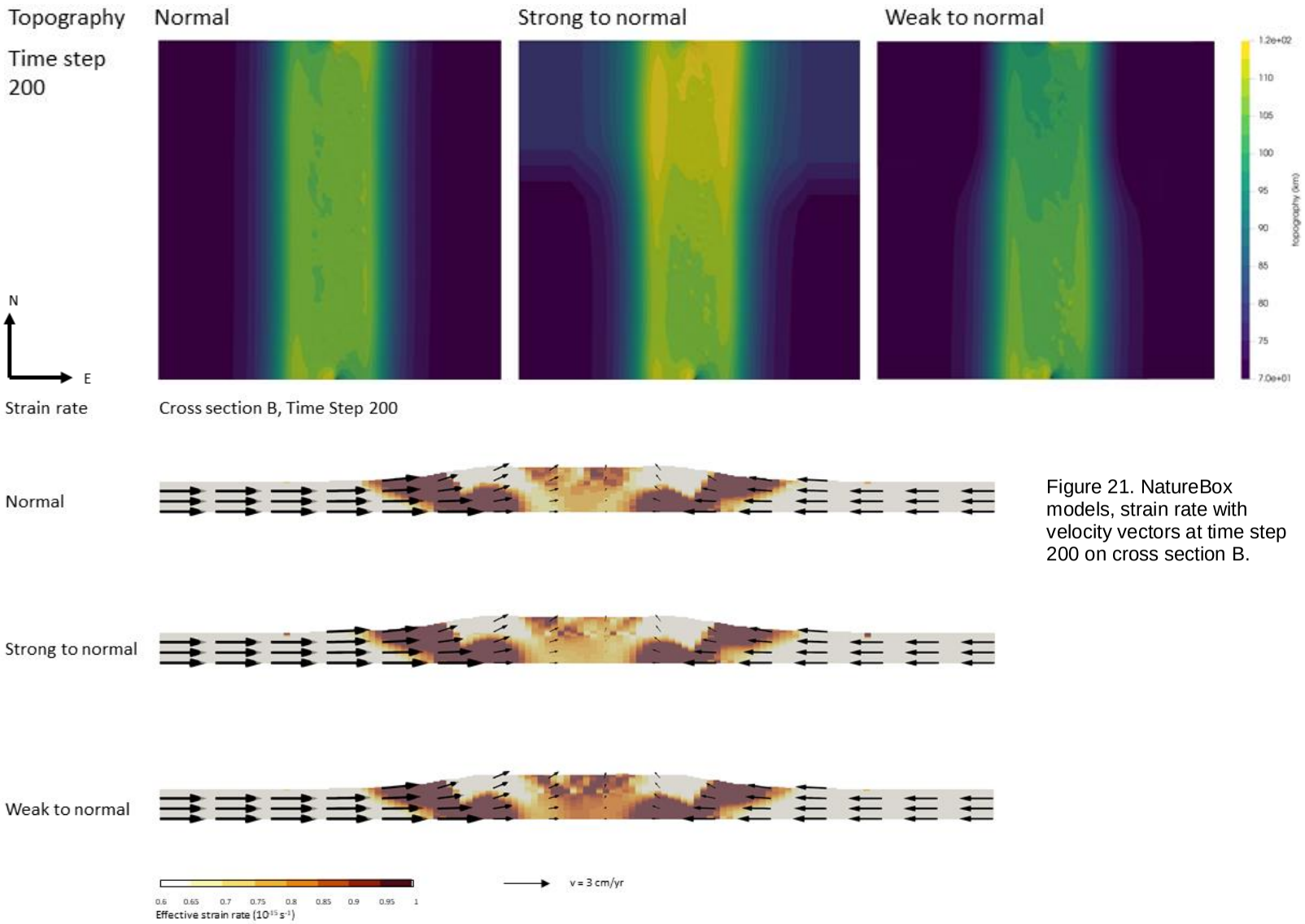

Figure 20. NatureBox models, vertical elevation above model base at time step 200.

Figure 21. NatureBox models, strain rate with velocity vectors at time step 200 on cross section B.

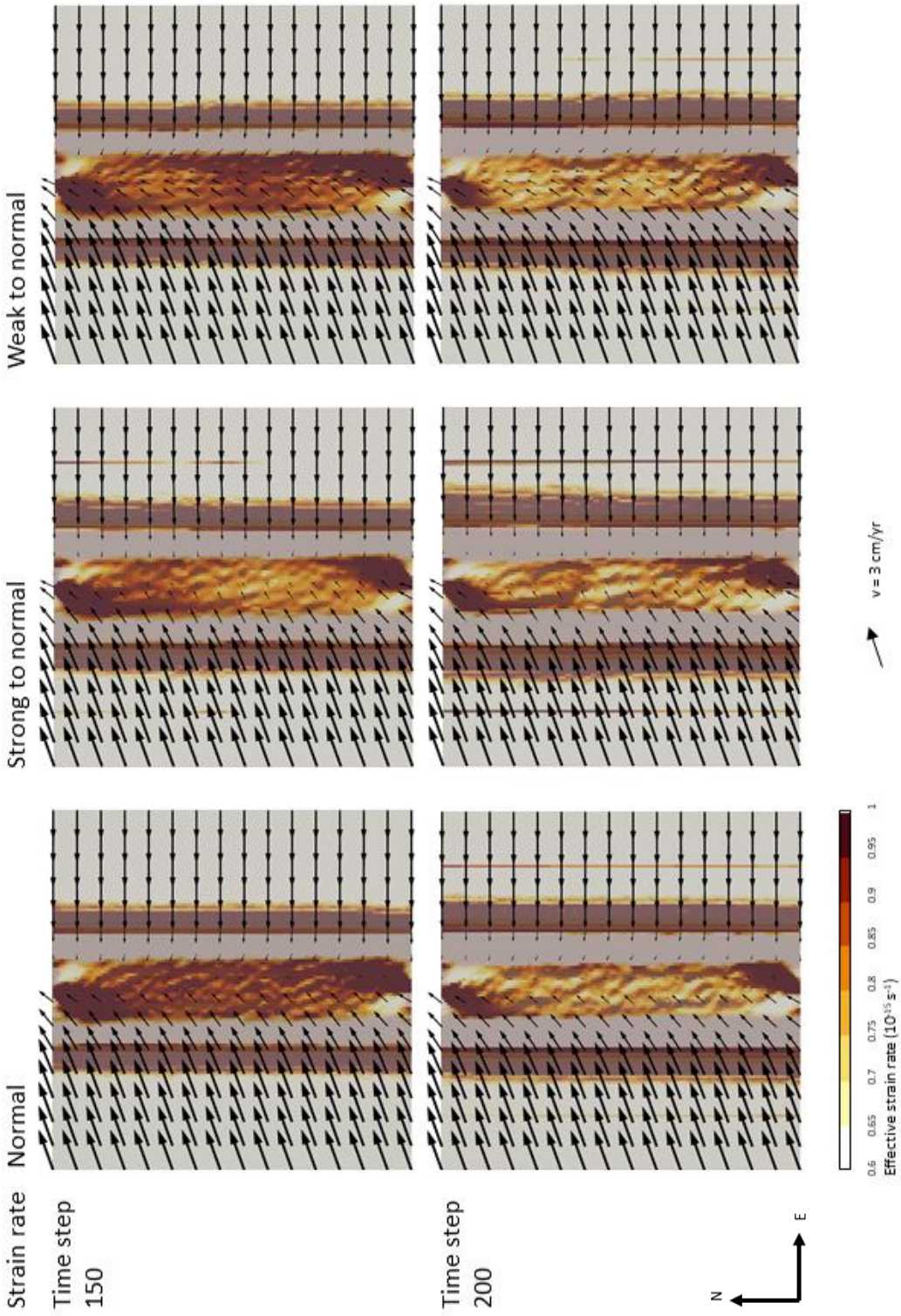

Figure 22. NatureBox models, strain rate with scaled velocity vectors at time step 150 and 200.

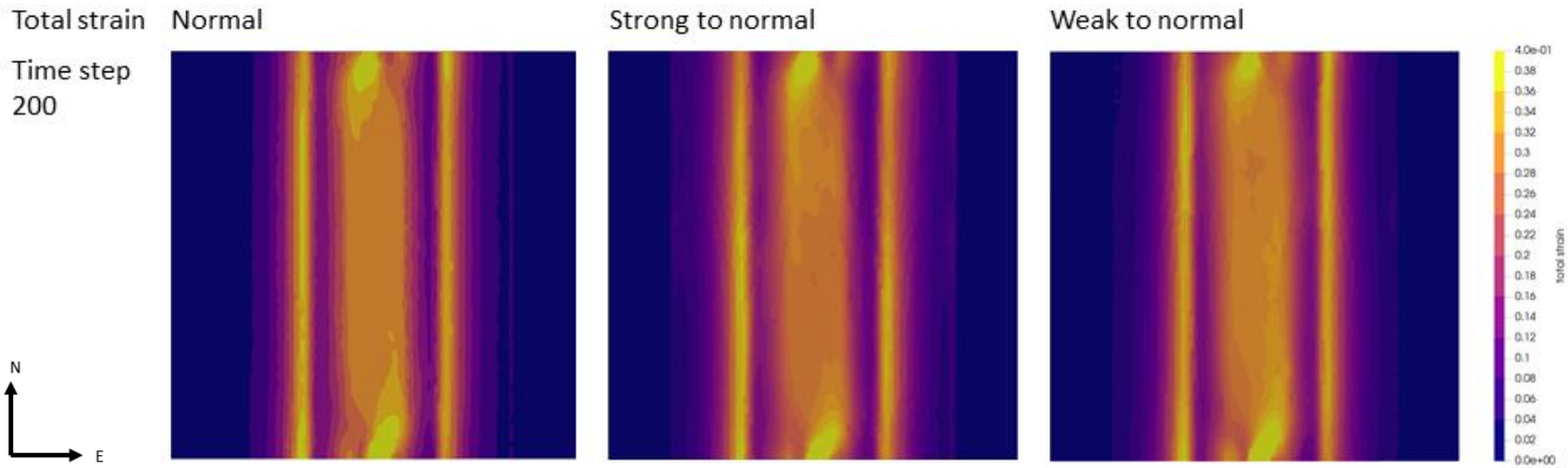

Figure 23. NatureBox models, accumulated strain at time step 200.

strain rate is generally low (Figure 25). The model with a dip angle of 30˚ appears to accommodate less strain at the subduction interface and has a larger partitioned component at the thrust fault than the model with a 50˚ dip. There is some along-strike variation in the strain rate at the weak zone in the steeply dipping model but there is no sign of the set of margin-oblique and margin-parallel faults that bound a rhomb-shaped domain as observed in the MultiBox and NatureBox models.

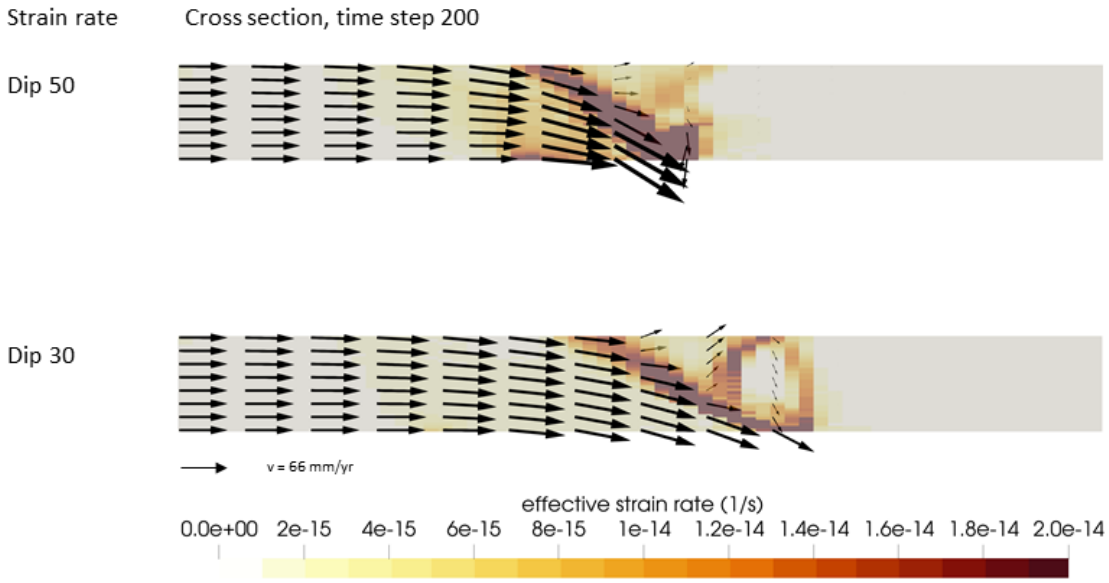

Figure 24. Natural System models with a dip angle of 50 and 30 degrees respectively: strain rate with velocity vectors at time step 200 is shown in a cross section taken at the middle of the model.

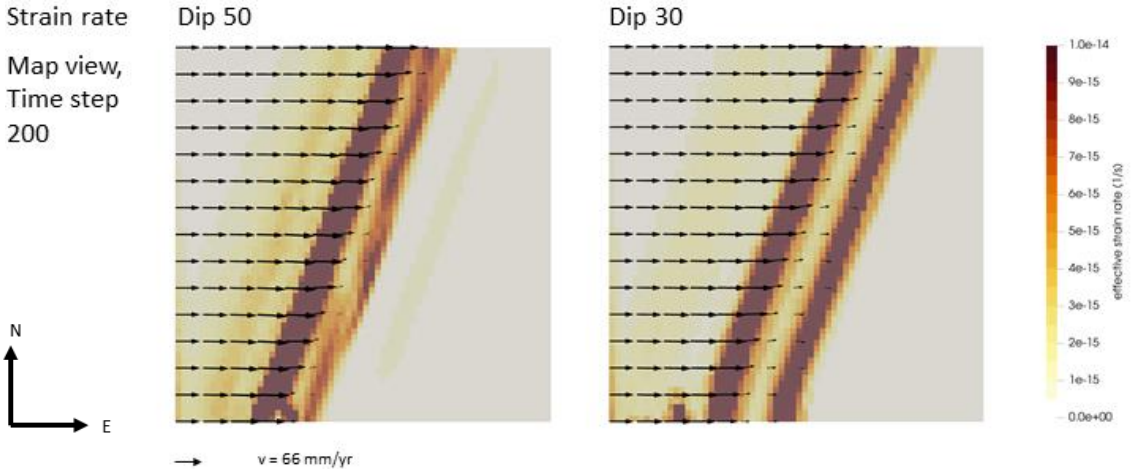

Figure 24. Natural System models with a dip angle of 50 and 30 degrees respectively: strain rate with velocity vectors at time step 200 is shown in map view.

4.3.2. Velocity vectors

In the fore-arc region, the velocity is NE-oriented as applied (as in Figure 3) and there is a small trench-ward motion in the back-arc region (Figure 26 and 27). Northward and eastward velocities both distribute uniformly across the width of the area bounded by the subduction interface and the weak zone and shows no along-strike variation as well (Figure 26 and 27). There is also northward transport of material in the fore-arc region in both models directly to the east of the trench, and the northward velocity decreases farther eastward towards the location of the weak zone and farther into the back-arc region, which shows weak partitioning of strain in the area. The existence of southward velocity component is likely to be related to the velocity vectors rotating to be perpendicular to the boundary between the weak zone and the interior of the continent.

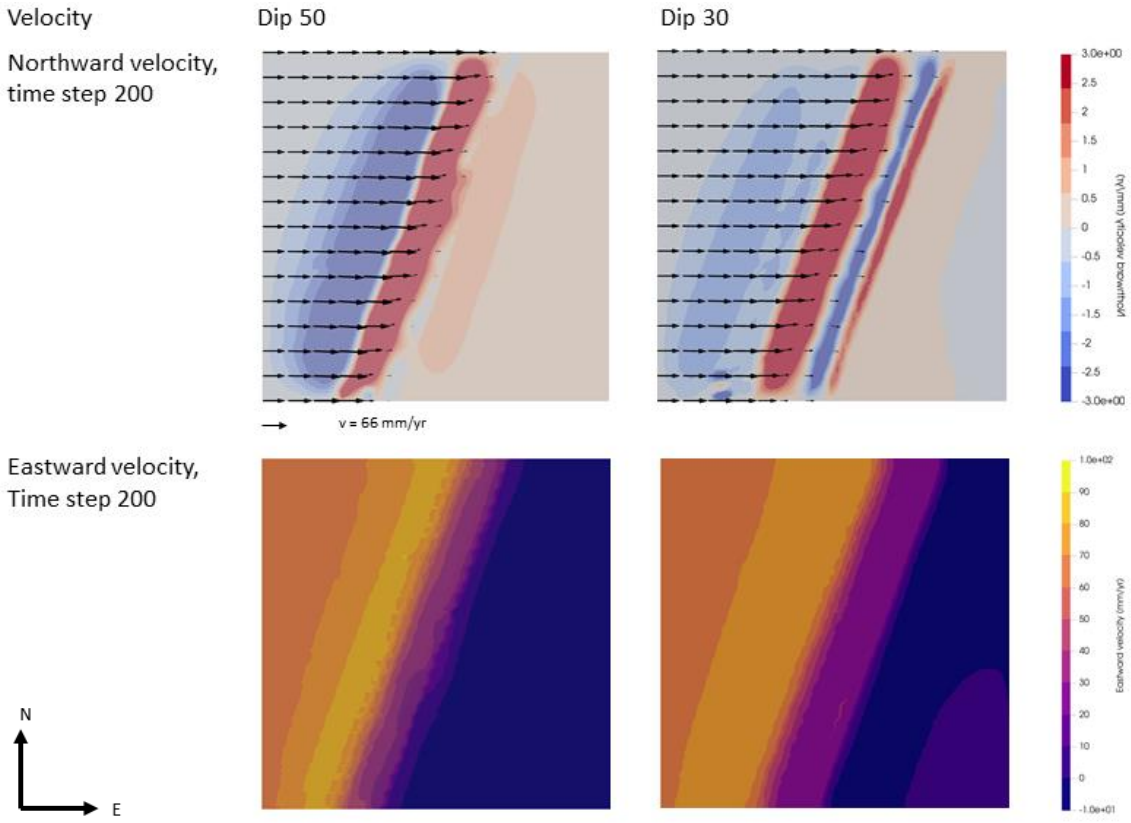

Figure 26. Natural System models with a dip angle of 50 and 30 degrees respectively: northward and east ward velocity at time step 200 is shown in a map view.

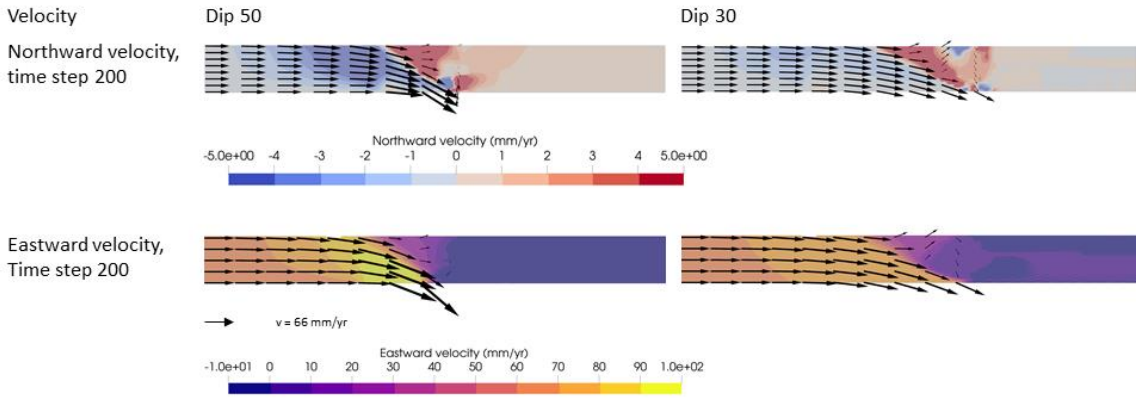

Figure 27. Natural System models with a dip angle of 50 and 30 degrees respectively: northward and east ward velocity with velocity vectors at time step 200 is shown in a cross section taken at the middle of the model.

5. DISCUSSION

The results from the numerical MultiBox and NatureBox models are generally comparable to each other and to the analog models of Eisermann et al. (2018). Apart from this similarity, the Natural System models do not show the same displacement patterns and structures, especially the margin-oblique faults that were expected (Figure 25).

5.1. Comparison of the Analog Models to Their Numerical Equivalents

A lot of the qualitative findings of the analog models are successively reproduced in our numerical models. For example, the vertical uplift is greatest in the two anticlines that form at the velocity discontinuities on both sides of the central deformation zone (Figure 12 and 20) as described by Eisermann et al. (2018). The anticlines also sit on top of a set of thrust faults which extend downward and converge to form a pop-up structure. Strain rate is accommodated within a wide central deformation zone and on NW-oriented margin-oblique faults (Figure 14-15 and 21-22). The set of margin-oblique and margin-parallel faults enclose rhomb-shaped domains inside the deformation zone. With the similarities mentioned above, we can also say that the model results are similar to what is observed in the LOFZ area, where the stress is accommodated by both the margin-parallel main branch of LOFZ and conjugate sets of faults with different orientation including the NW-oriented margin-oblique faults (Perez et al. 2016; Sielfeld et al. 2018).

This displacement field of these numerical models matches the observation in Eisermann et al. (2018) as well. There is clockwise rotation on the velocity vectors on the east section of the central deformation zone, compared to a small counter-clockwise rotation on the western section of the central deformation zone (Figure 14-15 and 21-22). This rotation is present in all sections of the models. There is also a northward transport of material in all models with and without a thickness gradient, except that the material movement is southward in the transition zone in the strong-to-normal model. As concluded by Eisermann et al. (2018), the change in crustal thickness is important in that the southward transport of material initiates at the boundary of transition zone. The change in direction of velocity vectors at the northern boundary of the LOFZ from NE-oriented to SE-oriented (Moreno et al. 2011) also spatially coincides with the change in crustal thickness and slab dip (Ramos et al. 1999; Cembrano and Lara, 2009; Pesicek et al. 2012).

Rhomb-shaped domains inside the central deformation zone are present in the MultiBox and NatureBox models even when there is no along-strike variation in crustal thickness (Figure 15 and 22), which is also the same in the MultiBox analog models (Eisermann et al. 2018). They are bounded by margin-oblique faults that cross-cut the central deformation zone, together with margin-parallel bounding faults or shorter ones that fragmented the oblique faults. This complex fault system is captured in all MultiBox and NatureBox models, only with different size or resolution. The two weak-to-normal models use a different surface type due to the limit of the current definition of the surface used by the strong-to-normal models. It will be best if these two sets of models are implemented with the same boundary condition.

5.2. Comparison of the NatureBox and MultiBox Models: Any scaling effects?

Comparing the result from NatureBox and MultiBox models, the deformation and displacement pattern is generally similar, while the exact pattern is not the same. In both sets of models, two thrust fronts form in the fore-arc and back-arc region, while multiple shear zones in the central deformation zone accommodates most convergence strain. The rhomb-shaped domains are present in both sets of models, but the margin-oblique faults bounding the domains are not as well-developed in the NatureBox models as in the MultiBox models (Figure 15 and 22). They are more often fragmented into shorter segments by the margin-parallel faults (Figure 22) rather than crosscutting the full width

of the central deformation area (Figure 15). We have known that in geodynamical modelling, scaling the density to resemble the natural system could be problematic and might be the cause of this difference between the NatureBox and MultiBox result (Allen and Beaumont, 2012).

5.3. Comparison of the Natural System Models to the NatureBox Models

Despite the similarity between the analog MultiBox results and the numerical versions of them, the Natural System models do not show the same set of margin-parallel and margin-oblique faults cross-cutting the central deformation zone (Figure 25). There is slightly more interaction between the weak zone and subduction interface in the 50˚ dip model than the 30˚ dip model, but this could be associated with the closer distance between the trench and the weak zone. Considering the narrow width of the deformation zone, it is possible that insufficient model resolution limits the visible details in the area and structures similar to those observed in the MultiBox and NatureBox numerical models may thus not be observed.

If a stronger material is present in the continental crust of northern section of the model, the distribution of strain and velocity is generally similar to the models with uniform crustal strength (Figures 24-27 and 28-31). A slightly wider zone between the subduction interface and the weak zone related shear zone in models with both a steep (50˚) and a moderate (30˚) dip (Figures 28 and 29) compared to models without a thickness gradient (Figures 24 and 25). However, there is still no sign of the rhomb-shaped domains even with a greater distance between the shear zones. In the stronger section in both of these models, the region of northward transport of material is narrower than south of it, which indicates a narrower region of strain partitioning (Figure 30).

It is possible that the rhomb-shaped domains are only a product under the specific setting within the analog models and the numerical versions of them with a free-slip central region, considering that this difference between the Natural System models and the NatureBox models. There is also no evidence that suggest a freely-deforming layer underlying the Southern Andes, so the origin of this tectonic behavior remains a mystery.

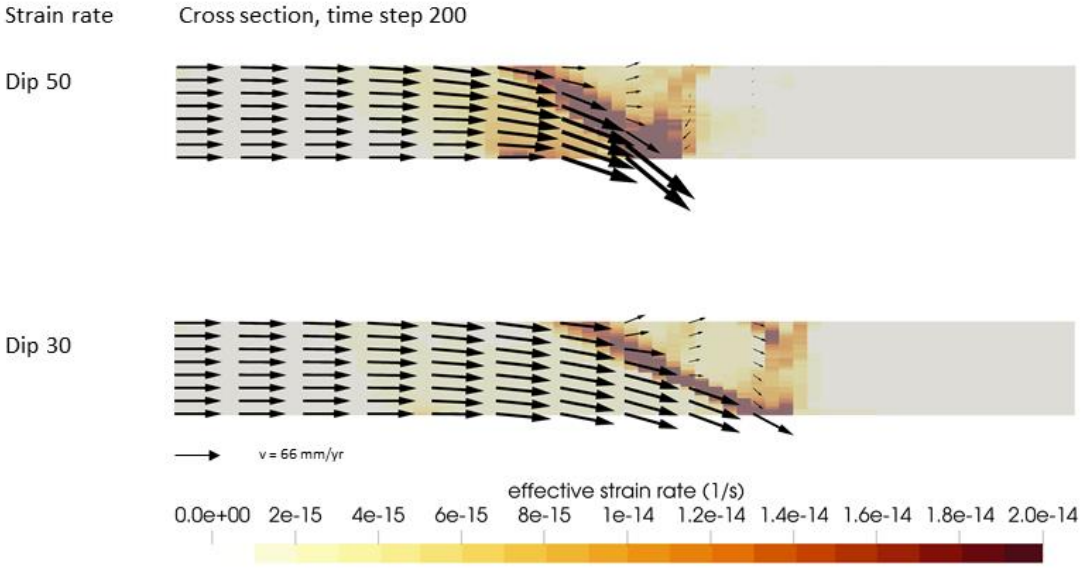

Figure 28. Natural System models with a stronger northern section: strain rate with velocity vectors at time step 200 is shown in a cross section taken at the middle of the model.

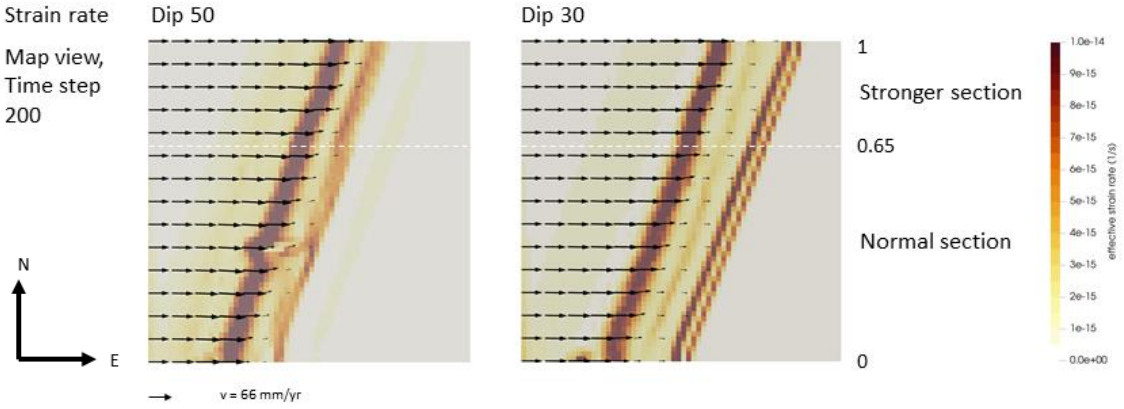

Figure 29. Natural System models with a stronger northern section: strain rate with velocity vectors at time step 200 is shown in map view.

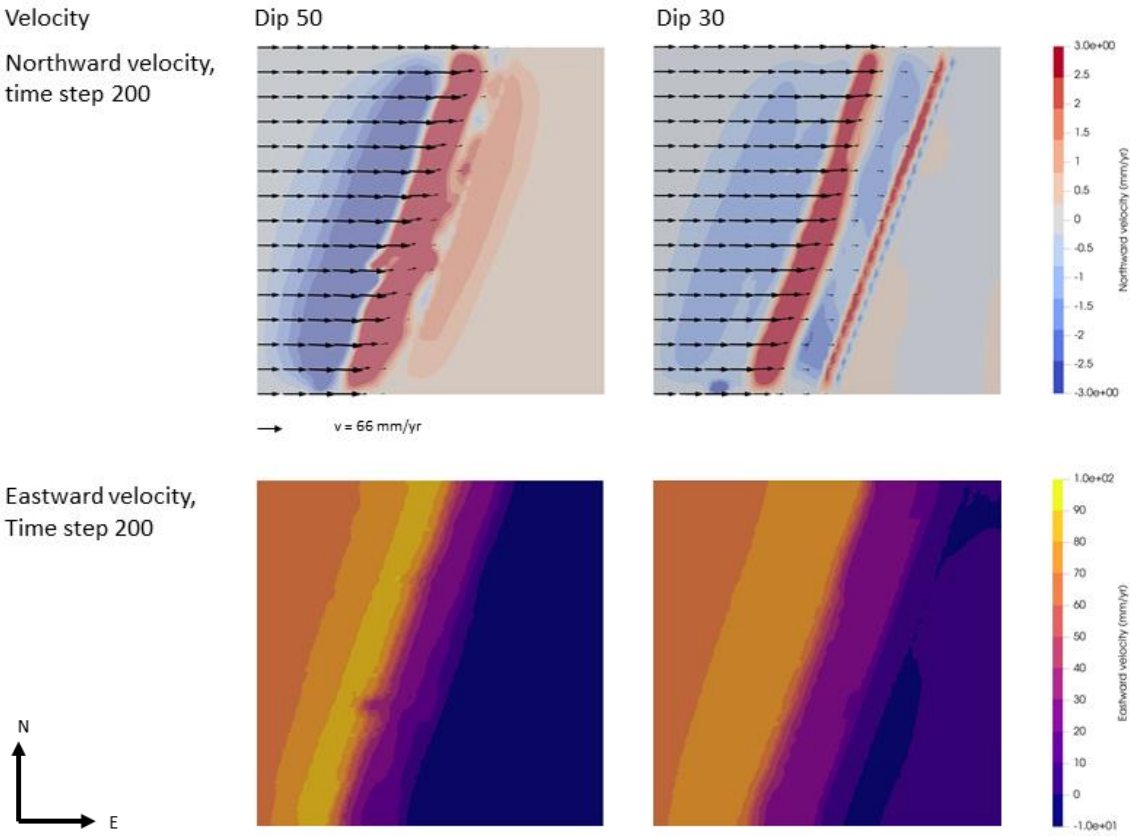

Figure 30. Natural System models with a stronger northern section: northward and east ward velocity with velocity vectors at time step 200 is shown in a map view.

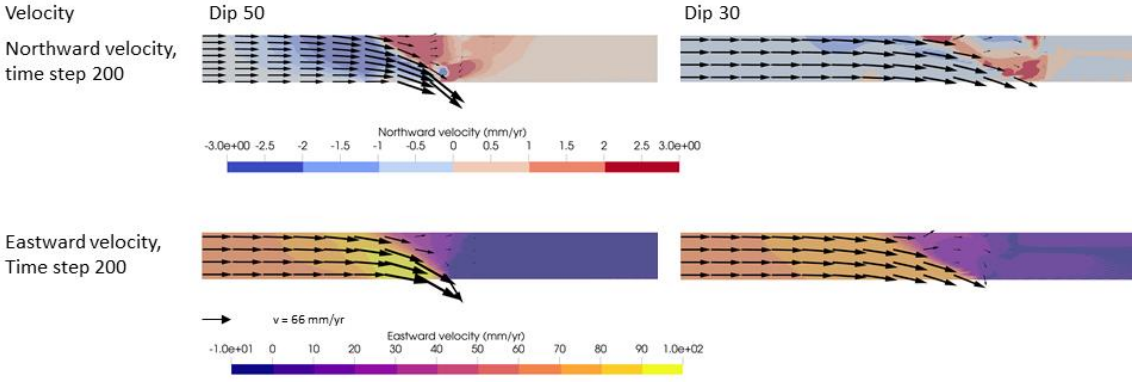

Figure 31. Natural System models with a stronger northern section: northward and east ward velocity with velocity vectors at time step 200 is shown in a cross section taken at the middle of the model.

5.4. Natural System Models and their relationship to the LOFZ

There is still some similarity between our Natural System model and the deformation pattern in the LOFZ. We observe a northward transport of material in the fore-arc region and a weak partitioning of strain in the area. The velocity fields match the GPS velocity of the LOFZ region, with the fore-arc accommodating the NE-oriented oblique convergence vector and a small back-arc trench-ward motion (Moreno et al. 2011). However, the complex margin-oblique and margin-parallel fault system and the change in displacement field as shown in Figure 3 is not present in any of the Natural System models.

5.5. Future Work

The study question is not fully explored by this thesis and there is still a lot of possible improvements that can be implemented and many other hypotheses to be tested. The change in crustal thickness of the strong-to-normal and weak-to-normal models in both the MultiBox and NatureBox series are implemented with different DOUAR surface types due to limitation of the original surface definition in the program. It will be most desirable if they are implemented with the same surface type in the future. While our simple Natural System models do not develop the rhomb-shaped domains bounded by conjugate sets of faults as observed in the LOFZ either with and without a stronger northern section and both with a 50 and 30 dip, we should consider other possibilities that might be related to this complex feature of the LOFZ. If sufficient computational resources were available, it would be interesting to run all models at a higher resolution to explore the small and complex fault systems.

6. CONCLUSIONS

In general, the numerical modelling results of this project are comparable to the analog MultiBox experiments (Eisermann et al. 2018). The results from analog models are reproducible using numerical models with similar boundary conditions and material properties. Numerical modelling is thus a suitable way to study the reproducibility of

analog models and to study the change in strain rate and stress throughout a 3D body. We confirmed that the set of margin-oblique and margin-parallel faults enclosing a rhomb shaped domain is present in the central deformation zone of all numerical versions of analog model experiments, and we also confirmed that a change in velocity vector orientation that is similar to the GPS velocity at the northern terminus of the LOFZ is observed in the strong-to-normal models.

However, the Natural System models do not show the same complex features inside the deformation zone related to the weak zone as observed in numerical versions of the analog model. We have tested different material properties and boundary conditions and find that the model with a 30° subduction dip and stronger northern section has the velocity vectors rotated from NE to SE starting at the transition in material strength. In the future, models with a higher resolution and other boundary conditions could be implemented to study the stress partitioning in the LOFZ.

7. APPENDIX A: Numerical modelling with DOUAR

Numerical modelling of oblique subduction system is studied using DOUAR (Braun et al. 2008; Thieulot et al. 2008), which involves solving the equation of conservation of momentum from the 3-D Stokes equations:

$$\nabla \cdot \eta(\nabla \mathrm{V} + \nabla \mathrm{V}^{\mathrm{T}}) - \nabla P = \rho g \ ,$$

where η is the fluid shear viscosity, V is fluid velocity, V^{T} is transpose matrix of fluid velocity, P is pressure (mean stress), ρ is the fluid density, and g is the gravitational acceleration. Since an incompressibility assumption is made for the fluid material, we also have:

$$\nabla \cdot \mathrm{V} = 0 \ ,$$

where $\nabla \cdot \mathrm{V}$ is the divergence of the velocity. Pressure is thus calculated with a penalty factor λ (Bathe, 1982, and references therein):

$$\mathrm{P} = -\lambda \nabla \cdot \mathrm{V} \ ,$$

which treats the fluid as nearly incompressible with a λ that is usually 8 orders of magnitude larger than η. Rock rheology in DOUAR is either linear viscous (Newtonian) or viscous-plastic. Plastic material is implemented with a Mohr-coulomb failure criterion calculated with stress tensor invariants:

$$J_1 = \sigma_{ii}$$

$$J_2' = \frac{1}{2}\sigma_{ij}'\sigma_{ij}'$$

$$J_3' = \frac{1}{3}\sigma_{ij}'\sigma_{jk}'\sigma_{ki}' \ ,$$

where i, j, and k are symbolic coordinate indices. J_1 is the first invariant of the Cauchy stress tensor σ, and J_2' and J_3' are the second and third invariants of the deviatoric stress tensor σ' :

$$\sigma' = \sigma - J_1'\delta_{ij} \ ,$$

where δ_{ij} is the Kronecker delta. The Mohr-Coulomb criterion can now be defined with the stress invariants:

$$F = \frac{1}{3}J_1 \sin(\phi) + \sqrt{J_2'}\left(\cos(\theta_L) - \frac{1}{\sqrt{3}}\sin(\phi)\cos(\theta_L)\right) - c\cos(\phi) = 0 \ ,$$

where ϕ is the angle of internal friction and θ_L is the Lode angle defined as:

$$\theta_L = \frac{1}{3}\sin^{-1}\left(\frac{-3\sqrt{3}}{2}\frac{J_3'}{J_2'^{\frac{3}{2}}}\right) .$$

DOUAR calculates stresses from the strain rate tensor invariants:

$$I_1 = \acute{\varepsilon}_{ii}$$

$$I_2' = \frac{1}{2}\acute{\varepsilon}_{ij}'\acute{\varepsilon}_{ij}'$$

$$I_3' = \frac{1}{3}\dot{\varepsilon}_{ij}'\dot{\varepsilon}_{jk}'\dot{\varepsilon}_{ki}' .$$

I_1 is the first invariant of the strain rate tensor $\dot{\varepsilon}$, and I_2' and I_3' are the second and third invariants of the deviatoric strain rate tensor $\dot{\varepsilon}'$ defined as:

$$\dot{\varepsilon}' = \dot{\varepsilon} - \frac{1}{3}I_1\delta_{ij} .$$

The strain rate and deviatoric strain rate tensor will be the same if the material is incompressible ($I_1 = 0$). During each model iteration, the elemental effective viscosity $\sqrt{J_2'}$ is calculated with:

$$\sqrt{J_2'} = 2\eta\sqrt{I_2'} .$$

When the elemental effective stress exceeds the Mohr-Coulomb yield strength σ_y , the element is on yield and the effective shear viscosity η_{eff} is recalculated as:

$$\eta_{eff} = \frac{\sigma_y}{2\sqrt{I_2'}} .$$

When the elemental effective stress is below yield strength, the initial viscosity is used.

8. APPENDIX B

Following the work of Schütt and Whipp (2020), the parabola definition of the subduction interface uses the following equation as in Figure B1:

$$z = a(x - d)^2 + c$$

where x is the distance along the x-axis, z is the distance along the z-axis, $a = (z_{min} - z_{max})/(x_{end} - x_{start})$, $c = z_{max}$, and $d = x_{start}$. z_{min} and z_{max} define the vertical location where subduction of material is happening and in the Natural System models described above, $z_{min} = 0$ and $z_{max} = 100$ km, which cover all of the incoming oceanic plate. $x_{start} = 0$ and the value of x_{end} is the distance along the x-axis between the start and end of the parabola, which controls the dip angle. In the Natural System model, the subduction dip angle is approximated as the angle of the triangle inside the parabola (Figure B1).

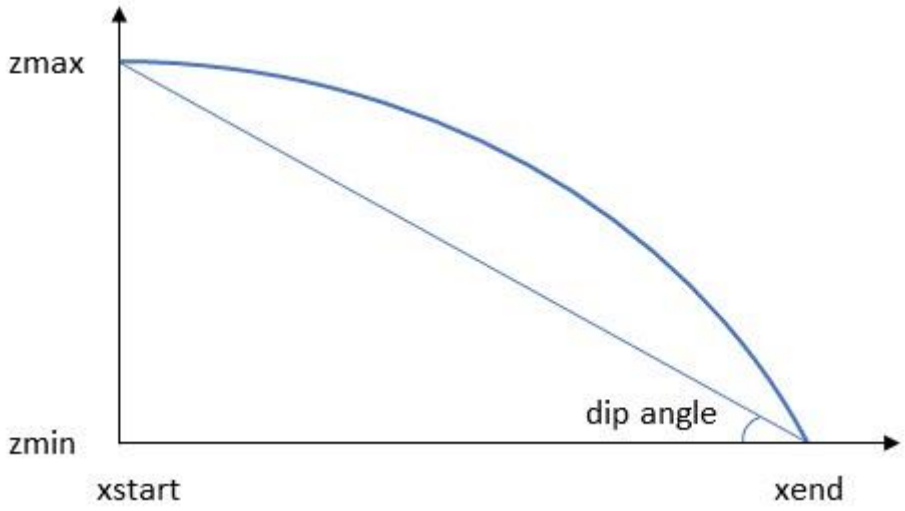

Figure B1. Illustration on definition of the subduction interface as a parabola.

9. REFERENCES

Allen, J., & Beaumont, C. (2012). Impact of inconsistent density scaling on physical analogue models of continental margin scale salt tectonics. Journal of Geophysical Research-Solid Earth, 117. https://doi.org/Artn B0810310.1029/2012jb009227

Alvarado, A., Audin, L., Nocquet, J. M., Jaillard, E., Mothes, P., Jarrin, P., Segovia, M., Rolandone, F., & Cisneros, D. (2016). Partitioning of oblique convergence in the Northern Andes subduction zone: Migration history and the present-day boundary of the North Andean Sliver in Ecuador. Tectonics, 35(5), 1048-1065. https://doi.org/10.1002/2016tc004117

Angermann, D., Klotz, J., & Reigber, C. (1999). Space-geodetic estimation of the Nazca-South America Euler vector. Earth and Planetary Science Letters, 171(3), 329-334. https://doi.org/Doi 10.1016/S0012-821x(99)00173-9

Barazangi, M., & Isacks, B. L. (1976). Spatial distribution of earthquakes and subduction of the Nazca plate beneath South America. Geology, 4(11), 686-692. https://doi.org/10.1130/0091-7613(1976)4<686:SDOEAS>2.0.CO;2

Bathe, K.-J. (1982). Finite element procedures in engineering analysis. Englewood Cliffs, NJ: Prentice-Hall.

Beck, M. E. (1983). On the Mechanism of Tectonic Transport in Zones of Oblique Subduction. Tectonophysics, 93(1-2), 1-11. https://doi.org/Doi 10.1016/0040-1951(83)90230-5

Beck, M. E., Rojas, C., & Cembrano, J. (1993). On the Nature of Buttressing in Margin-Parallel Strike-Slip-Fault Systems. Geology, 21(8), 755-758. <Go to ISI>://WOS:A1993LR57200021

Benioff, Hugo (1949). "Seismic evidence for the fault origin of oceanic deeps". Bulletin of the Geological Society of America. 60 (12): 1837–1866. Bibcode:1949GSAB...60.1837B. doi:10.1130/0016-7606(1949)60[1837:seftfo]2.0.co;2.

Bishop, B. T., Beck, S. L., Zandt, G., Wagner, L., Long, M., Antonijevic, S. K., Kumar, A., & Tavera, H. (2017). Causes and consequences of flat-slab subduction in southern Peru. Geosphere, 13(5), 1392-1407. https://doi.org/10.1130/Ges01440.1

Braun, J., Thieulot, C., Fullsack, P., DeKool, M., Beaumont, C., & Huismans, R. (2008). DOUAR: A new three-dimensional creeping flow numerical model for the solution of geological problems. Physics of the Earth and Planetary Interiors, 171(1-4), 76-91. https://doi.org/10.1016/j.pepi.2008.05.003

Burov, E., Francois, T., Yamato, P., & Wolf, S. (2014). Advances and challenges in geotectonic modelling. Bulletin De La Societe Geologique De France, 185(3), 147-169. https://doi.org/DOI 10.2113/gssgfbull.185.3.147

Cembrano, J., Gonzalez, G., Arancibia, G., Ahumada, I., Olivares, V., & Herrera, V. (2005). Fault zone development and strain partitioning in an extensional strike-slip duplex: A case study from the Mesozoic Atacama fault system, Northern Chile. Tectonophysics, 400(1-4), 105-125. https://doi.org/10.1016/j.tecto.2005.02.012

Cembrano, J., Gonzalez, G., Arancibia, G., Ahumada, I., Olivares, V., & Herrera, V. (2005). Fault zone development and strain partitioning in an extensional strike-slip duplex: A case study from the Mesozoic Atacama fault system, Northern Chile. Tectonophysics, 400(1-4), 105-125. https://doi.org/10.1016/j.tecto.2005.02.012

Cembrano, J., & Lara, L. (2009). The link between volcanism and tectonics in the southern volcanic zone of the Chilean Andes: A review. Tectonophysics, 471(1-2), 96-113. https://doi.org/10.1016/j.tecto.2009.02.038

Cobbold, P. R., Rossello, E. A., Roperch, P., Arriagada, C., Gomez, L. A., & Lima, C. (2007). Distribution, timing, and causes of Andean deformation across South America. Deformation of the Continental Crust: The Legacy of Mike Coward, 272, 321-343. https://doi.org/Doi 10.1144/Gsl.Sp.2007.272.01.17

Courant, R., Friedrichs, K., & Lewy, H. (1928). Über die partiellen Differenzengleichungen der mathematischen Physik. Mathematische Annalen, 100(1), 32-74. https://doi.org/10.1007/BF01448839

Demets, C., Gordon, R. G., Argus, D. F., & Stein, S. (1994). Effect of Recent Revisions to the Geomagnetic Reversal Time-Scale on Estimates of Current Plate Motions. Geophysical Research Letters, 21(20), 2191-2194. https://doi.org/Doi 10.1029/94gl02118

Dewey, J. F., & Lamb, S. H. (1992). Active tectonics of the Andes. Tectonophysics, 205(1), 79-95. https://doi.org/https://doi.org/10.1016/0040-1951(92)90419-7

Diraison, M., Cobbold, P. R., Rossello, E. A., & Amos, A. J. (1998). Neogene dextral transpression due to oblique convergence across the Andes of northwestern Patagonia, Argentina. Journal of South American Earth Sciences, 11(6), 519-532. https://doi.org/Doi 10.1016/S0895-9811(98)00032-7

Eisenstadt, G., & Sims, D. (2005). Evaluating sand and clay models: do rheological differences matter? Journal of Structural Geology, 27(8), 1399-1412. https://doi.org/10.1016/j.jsg.2005.04.010

Eisermann, J. O. (2018). Regional velocity field variations in the Southern Andes: evidence from scaled analogue experiments using the MultiBox (Unpublished master's thesis). Universität Hamburg, Hamburg, German.

Fitch, T. J. (1972). Plate Convergence, Transcurrent Faults, and Internal Deformation Adjacent to Southeast Asia and Western Pacific. Journal of Geophysical Research, 77(23), 4432-&. https://doi.org/DOI 10.1029/JB077i023p04432

Gansser, A. (1973). Facts and theories on the Andes: Twenty-sixth William Smith Lecture. Journal of the Geological Society, 129(2), 93-131. https://doi.org/10.1144/gsjgs.129.2.0093

Giggenbach, W. F. (1992). Seg Distinguished Lecture - Magma Degassing and Mineral Deposition in Hydrothermal Systems Along Convergent Plate Boundaries. Economic Geology and the Bulletin of the Society of Economic Geologists, 87(7), 1927-1944. <Go to ISI>://WOS:A1992JZ56300014

Gorring, M. L., Kay, S. M., Zeitler, P. K., Ramos, V. A., Rubiolo, D., Fernandez, M. I., & Panza, J. L. (1997). Neogene Patagonian plateau lavas: Continental magmas associated with ridge collision at the Chile Triple Junction. Tectonics, 16(1), 1-17. https://doi.org/Doi 10.1029/96tc03368

Gutscher, M. A., Spakman, W., Bijwaard, H., & Engdahl, E. R. (2000). Geodynamics of flat subduction: Seismicity and tomographic constraints from the Andean margin. Tectonics, 19(5), 814-833. https://doi.org/Doi 10.1029/1999tc001152

Hernandez-Moreno, C., Speranza, F., & Di Chiara, A. (2014). Understanding kinematics of intra-arc transcurrent deformation: Paleomagnetic evidence from the Liquine-Ofqui fault zone (Chile, 38-41 degrees S). Tectonics, 33(10), 1964-1988. https://doi.org/10.1002/2014tc003622

Hessler, A. M., & Sharman, G. R. (2018). Subduction zones and their hydrocarbon systems. Geosphere, 14(5), 2044-2067. https://doi.org/10.1130/Ges01656.1

Hippertt, J. (1999). Are S-C structures, duplexes and conjugate shear zones different manifestations of the same scale-invariant phenomenon? Journal of Structural Geology, 21(8-9), 975-984. https://doi.org/Doi 10.1016/S0191-8141(99)00047-4

Hoffmann-Rothe, A., Kukowski, N., Dresen, G., Echtler, H., Oncken, O., Klotz, J., Scheuber, E., & Kellner, A. (2006). Oblique Convergence along the Chilean Margin: Partitioning, Margin-Parallel Faulting and Force Interaction at the Plate Interface. In (pp. 125-146). https://doi.org/10.1007/978-3-540-48684-8_6

Hubbert, M. K. (1937). Theory of scale models as applied to the study of geologic structures. GSA Bulletin, 48(10), 1459-1520. https://doi.org/10.1130/GSAB-48-1459

Jarrard, R. D. (1986). Relations among Subduction Parameters. Reviews of Geophysics, 24(2), 217-284. https://doi.org/DOI 10.1029/RG024i002p00217

Jordan, T. E., Isacks, B., Ramos, V., & Allmendinger, R. (1983). Mountain building in the Central Andes. Episodes, 3, 20-26.

Kearey, P., Klepeis, K. A., & Vine, F. J. (2017). Global tectonics. John Wiley.

Kumar, A., Wagner, L. S., Beck, S. L., Long, M. D., Zandt, G., Young, B., Tavera, H., & Minaya, E. (2016). Seismicity and state of stress in the central and southern Peruvian flat slab. Earth and Planetary Science Letters, 441, 71-80. https://doi.org/10.1016/j.epsl.2016.02.023

Lallemand, S., Heuret, A., & Boutelier, D. (2005). On the relationships between slab dip, back-arc stress, upper plate absolute motion, and crustal nature in subduction zones. Geochemistry Geophysics Geosystems, 6. https://doi.org/Artn Q0900610.1029/2005gc000917

Lavenu, A., & Cembrano, J. (1999). Compressional- and transpressional-stress pattern for Pliocene and Quaternary brittle deformation in fore arc and intra-arc zones (Andes of Central and Southern Chile). Journal of Structural Geology, 21(12), 1669-1691. https://doi.org/Doi 10.1016/S0191-8141(99)00111-X

Manea, V. C., Manea, M., Ferrari, L., Orozco-Esquivel, T., Valenzuela, R. W., Husker, A., & Kostoglodov, V. (2017). A review of the geodynamic evolution of flat slab subduction in Mexico, Peru, and Chile. Tectonophysics, 695, 27-52. https://doi.org/10.1016/j.tecto.2016.11.037

McCaffrey, R. (1992). Oblique plate convergence, slip vectors, and forearc deformation [https://doi.org/10.1029/92JB00483]. Journal of Geophysical Research: Solid Earth, 97(B6), 8905-8915. https://doi.org/https://doi.org/10.1029/92JB00483

Melnick, D., Folguera, A., & Ramos, V. A. (2006). Structural control on arc volcanism: The Caviahue-Copahue complex, Central to Patagonian Andes transition (38 degrees S). Journal of South American Earth Sciences, 22(1-2), 66-88. https://doi.org/10.1016/j.jsames.2006.08.008

Moreno, M., Melnick, D., Rosenau, M., Bolte, J., Klotz, J., Echtler, H., Baez, J., Bataille, K., Chen, J., Bevis, M., Hase, H., & Oncken, O. (2011). Heterogeneous plate locking in the South-Central Chile subduction zone: Building up the next great earthquake. Earth and Planetary Science Letters, 305(3-4), 413-424. https://doi.org/10.1016/j.epsl.2011.03.025

Müller, R. D., Zahirovic, S., Williams, S. E., Cannon, J., Seton, M., Bower, D. J., Tetley, M. G., Heine, C., Le Breton, E., Liu, S., Russell, S. H. J., Yang, T., Leonard, J., & Gurnis, M. (2019). A Global Plate Model Including Lithospheric Deformation Along Major Rifts and Orogens Since the Triassic [https://doi.org/10.1029/2018TC005462]. Tectonics, 38(6), 1884-1907. https://doi.org/https://doi.org/10.1029/2018TC005462

Nocquet, J. M., Villegas-Lanza, J. C., Chlieh, M., Mothes, P. A., Rolandone, F., Jarrin, P., Cisneros, D., Alvarado, A., Audin, L., Bondoux, F., Martin, X., Font, Y., Regnier, M., Vallee, M., Tran, T., Beauval, C., Mendoza, J. M. M., Martinez, W., Tavera, H., & Yepes, H. (2014). Motion of continental slivers and creeping subduction in the northern Andes. Nature Geoscience, 7(4), 287-291. https://doi.org/10.1038/ngeo2099

Oncken, O., Chong, G., Franz, G., Giese, P., Götze, H.-J., Ramos, V., Strecker, M., & Wigger, P. (2006). The Andes: Active Subduction Orogeny. https://doi.org/10.1007/978-3-540-48684-8

Pérez-Flores, P., Cembrano, J., Sánchez-Alfaro, P., Veloso, E., Arancibia, G., & Roquer, T. (2016). Tectonics, magmatism and paleo-fluid distribution in a strike-slip setting: Insights from the northern termination of the Liquiñe–Ofqui fault System, Chile. Tectonophysics, 680, 192-210. https://doi.org/https://doi.org/10.1016/j.tecto.2016.05.016

Pesicek, J. D., Engdahl, E. R., Thurber, C. H., DeShon, H. R., & Lange, D. (2012). Mantle subducting slab structure in the region of the 2010 M8.8 Maule earthquake (30-40 degrees S), Chile. Geophysical Journal International, 191(1), 317-324. https://doi.org/10.1111/j.1365-246X.2012.05624.x

Philippon, M., & Corti, G. (2016). Obliquity along plate boundaries. Tectonophysics, 693, 171-182. https://doi.org/10.1016/j.tecto.2016.05.033

Ramos, V. A. (1999). Plate tectonic setting of the Andean Cordillera. Episodes, 22(3), 183-190. <Go to ISI>://WOS:000083727000005

Ramos, V. A., & Kay, S. M. (1992). Southern Patagonian Plateau Basalts and Deformation - Backarc Testimony of Ridge Collisions. Tectonophysics, 205(1-3), 261-282. https://doi.org/Doi 10.1016/0040-1951(92)90430-E

Reber, J. E., Cooke, M. L., & Dooley, T. P. (2020). What model material to use? A Review on rock analogs for structural geology and tectonics. Earth-Science Reviews, 202. https://doi.org/ARTN 10310710.1016/j.earscirev.2020.103107

Rosenau, M., Melnick, D., & Echtler, H. (2006). Kinematic constraints on intra-arc shear and strain partitioning in the southern Andes between 38 degrees S and 42 degrees S latitude. Tectonics, 25(4). https://doi.org/Artn Tc401310.1029/2005tc001943

S.J.H, B., Babeyko, A., Ellis, S., T.V, G., Kaus, B., Kellner, A., Schreurs, G., & Yamada, Y. (2006). The numerical sandbox: Comparison of model results for a shortening and an extension experiment. In (Vol. 253, pp. 29-64). https://doi.org/10.1144/GSL.SP.2006.253.01.02

Schellart, W. P., & Strak, V. (2016). A review of analogue modelling of geodynamic processes: Approaches, scaling, materials and quantification, with an application to subduction experiments. Journal of Geodynamics, 100, 7-32. https://doi.org/10.1016/j.jog.2016.03.009

Schutt, J. M., & Whipp, D. M. (2020). Controls on Continental Strain Partitioning Above an Oblique Subduction Zone, Northern Andes. Tectonics, 39(4). https://doi.org/10.1029/2019tc005886

Schreurs, G., Buiter, S. J. H., Boutelier, D., Corti, G., Costa, E., Cruden, A. R., Daniel, J.-M., Hoth, S., Koyi, H. A., Kukowski, N., Lohrmann, J., Ravaglia, A., Schlische, R. W., Withjack, M. O., Yamada, Y., Cavozzi, C., Del Ventisette, C., Brady, J. A. E., Hoffmann-Rothe, A., Mengus, J.-M., Montanari, D., & Nilforoushan, F. (2006). Analogue benchmarks of shortening and extension experiments. In S. J. H. Buiter & G. Schreurs (Eds.), Analogue and Numerical Modelling of Crustal-Scale Processes (Vol. 253, pp. 0). Geological Society of London. https://doi.org/10.1144/GSL.SP.2006.253.01.01

Sielfeld, G., Lange, D., & Cembrano, J. (2019). Intra-Arc Crustal Seismicity: Seismotectonic Implications for the Southern Andes Volcanic Zone, Chile [https://doi.org/10.1029/2018TC004985]. Tectonics, 38(2), 552-578. https://doi.org/https://doi.org/10.1029/2018TC004985

Stern, R. J. (2002). SUBDUCTION ZONES [https://doi.org/10.1029/2001RG000108]. Reviews of Geophysics, 40(4), 3-1-3-38. https://doi.org/https://doi.org/10.1029/2001RG000108

Thieulot, C., Fullsack, P., & Braun, J. (2008). Adaptive octree-based finite element analysis of two- and three-dimensional indentation problems. Journal of Geophysical Research-Solid Earth, 113(B12). https://doi.org/Artn B1220710.1029/2008jb005591

van Hunen, J., & Moyen, J. F. (2012). Archean Subduction: Fact or Fiction? Annual Review of Earth and Planetary Sciences, Vol 40, 40, 195-219. https://doi.org/10.1146/annurev-earth-042711-105255

Viola, G., Odonne, F., & Mancktelow, N. S. (2004). Analogue modelling of reverse fault reactivation in strike-slip and transpressive regimes: application to the Giudicarie fault system, Italian Eastern Alps. Journal of Structural Geology, 26(3), 401-418. https://doi.org/10.1016/j.jsg.2003.08.014

Wang, K., Hu, Y., Bevis, M., Kendrick, E., Smalley, R., & Lauria, E. (2007). Crustal motion in the zone of the 1960 Chile earthquake: Detangling earthquake-cycle deformation and forearc-sliver translation. Geochemistry Geophysics Geosystems, 8. https://doi.org/Artn Q1001010.1029/2007gc001721

Wilson, J. T. (1966). Did the Atlantic Close and then Re-Open? Nature, 211(5050), 676-681. https://doi.org/10.1038/211676a0